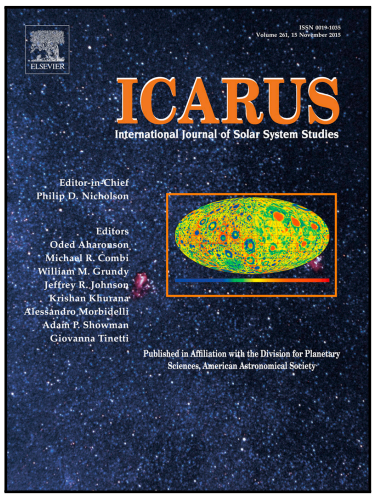

Ring faults and ring dikes around the Orientale basin on the Moon

Jeffrey C. Andrews-Hanna , James W. Head , Brandon Johnson , James T. Keane , Walter S. Kiefer , Patrick J. McGovern , Gregory A. Neumann , Mark A. Wieczorek , Maria T. Zuber

PII: S0019-1035(17)30581-X
DOI: 10.1016/j.icarus.2017.12.012
Reference: YICAR 12732

To appear in: *Icarus*

Received date: 10 August 2017
Revised date: 17 November 2017
Accepted date: 7 December 2017

Please cite this article as: Jeffrey C. Andrews-Hanna , James W. Head , Brandon Johnson , James T. Keane , Walter S. Kiefer , Patrick J. McGovern , Gregory A. Neumann , Mark A. Wieczorek , Maria T. Zuber , Ring faults and ring dikes around the Orientale basin on the Moon, *Icarus* (2017), doi: 10.1016/j.icarus.2017.12.012

Highlights

- High-resolution GRAIL gravity data reveals the structure of the Orientale basin
- Gravity gradients reveal a large ring dike intruded into the Outer Rook ring fault
- Crustal thickness models show ring faults extending to the crust-mantle interface

Ring faults and ring dikes around the Orientale basin on the Moon

Jeffrey C. Andrews-Hanna[1], James W. Head[2], Brandon Johnson[2], James T. Keane[3], Walter S. Kiefer[4], Patrick J. McGovern[4], Gregory A. Neumann[5], Mark A. Wieczorek[6], Maria T. Zuber[7]

[1]Lunar and Planetary Laboratory, University of Arizona, Tucson, AZ 85721-0092, USA.

[2]Department of Earth, Environmental, and Planetary Sciences, Brown University, Providence, RI 02912, USA

[3]Division of Geological and Planetary Sciences, California Institute of Technology, Pasadena, CA 91125, USA

[4]Lunar and Planetary Institute, University Space Research Association, Houston, TX 77058, USA.

[5]Solar System Exploration Division, NASA Goddard Space Flight Center, Greenbelt, MD 20771, USA.

[6]Université Côte d'Azur, Observatoire de la Côte d'Azur, CNRS, Laboratoire Lagrange, France

[7]Department of Earth, Atmospheric and Planetary Sciences, Massachusetts Institute of Technology, Cambridge, MA 02139-4307, USA.

Abstract.

The Orientale basin is the youngest and best-preserved multiring impact basin on the Moon, having experienced only modest modification by subsequent impacts and volcanism. Orientale is often treated as the type example of a multiring basin, with three prominent rings outside of the inner depression: the Inner Rook Montes, the Outer Rook Montes, and the Cordillera. Here we use gravity data from NASA's Gravity Recovery and Interior Laboratory (GRAIL) mission to reveal the subsurface structure of Orientale and its ring system. Gradients of the gravity data reveal a continuous ring dike intruded into the Outer Rook along the plane of the fault associated with the ring scarp. The volume of this ring dike is ~18 times greater than the volume of all extrusive mare deposits associated with the basin. The gravity gradient signature of the Cordillera ring indicates an offset along the fault across a shallow density interface, interpreted to be the base of the low-density ejecta blanket. Both gravity gradients and crustal thickness models indicate that the edge of the central cavity is shifted inward relative to the equivalent Inner Rook ring at the surface. Models of the deep basin structure show inflections along the crust-mantle interface at both the Outer Rook and Cordillera rings, indicating that the basin ring faults extend from the surface to at least the base of the crust. Fault dips range from 13-22° for the Cordillera fault in the northeastern quadrant, to 90° for the Outer Rook in the northwestern quadrant. The fault dips for both outer rings are lowest in the northeast, possibly due to the effects of either the direction of projectile motion or regional gradients in pre-impact crustal thickness. Similar ring dikes and ring faults are observed around the majority of lunar basins.

1. Introduction

Multiring basins are the most common large-scale structures on the terrestrial planets (e.g., Spudis, 1993). They were first discovered using Earth-based visible-wavelength images of the Moon, which revealed multiple concentric rings of massifs and/or inward-facing scarps surrounding impact basins (Hartmann and Kuiper, 1962; Hartmann and Wood, 1971). Subsequently, multiring basins have also been documented on Earth (e.g., Gulick et al., 2013), Mercury (e.g. Fassett et al., 2012; Spudis and Guest, 1988), and Mars (e.g., Schultz and Frey, 1990), with different but possibly related structures found on icy satellites in the outer solar system (Melosh, 1982). Multiring basins are defined as those basins with three or more prominent rings surrounding a central depression, with those basins possessing only two rings classified as peak-ring basins (Baker et al., 2011; Hartmann and Wood, 1971). The outermost prominent topographic ring is described as the basin rim, though the crustal structure of the basins reveals that the outer edge of the zone of crust that was thinned by the impact typically corresponds to one of the inner two rings (Baker et al., 2017, 2012, 2011; Neumann et al., 2015b; Wieczorek and Phillips, 1999), while the outer rings likely form from the collapse of the transient cavity (Head, 2010, 1974; Johnson et al., 2016; Melosh and Mckinnon, 1978). The outermost rings are typically twice the diameter of the zone of crustal thinning as demarcated by the central positive Bouguer anomaly (Neumann et al., 2015b).

Of lunar multiring basins, Orientale is the youngest and best-preserved example (Head, 1974; Wilhelms, 1987), having been only minimally altered by subsequent impacts or volcanism. Topography data and images (Fig. 1a,b) show the basin to be surrounded by three prominent ring structures (see discussion of the morphology of the rings in Hartmann and Kuiper, 1962; Head, 1974; Wilhelms, 1987). The ring centroids and radii stated below are calculated from best-fit

circles to the rings (and their associated 1-standard-deviation range) as expressed in LOLA topography data (Smith et al., 2010), using the inward-facing scarp where one exists. The Inner Rook Montes consist of a set of prominent massifs that surround the central depression of the basin (centered at $-19.2^{+0.7}_{-0.7}$ °N $265.9^{+0.9}_{-0.7}$ °E, at a radius $r \sim 232^{+3.9}_{-2.6}$ km). The Outer Rook Montes (centered at $-19.2^{+0.9}_{-0.7}$ °N $265.9^{+0.9}_{-0.7}$ °E, $r \sim 310^{+4.1}_{-2.7}$ km) and Cordillera (centered at $-19.9^{+1.8}_{-1.8}$ °N $265.9^{+2.0}_{-2.0}$ °E, $r \sim 462.3^{+5.1}_{-1.6}$ km) are each expressed as inward-facing scarps. A fourth ring, the inner ring that surrounds the inner depression ($r \sim 160$ km; Nahm et al., 2013), is expressed as a rounded bench in cross-section that is markedly less prominent in its topographic signature than the other rings (Nahm et al., 2013), and may have formed due to the thermal contraction of the post-impact melt pool within the basin (Vaughan et al., 2013; Wilson and Head, 2011). Alternatively, the inner ring might be an analog of structures in the Crisium basin, which are interpreted as the surface expression of thrust faults bounding the uplifted mantle beneath the basin center (Byrne et al., 2015). The inner depression approximately corresponds with the central positive Bouguer anomaly (Neumann et al., 2015b; Zuber et al., 2016), centered at $-19.2^{+0.9}_{-0.7}$ °N $265.9^{+0.9}_{-0.7}$ °E, $r \sim 172.4^{+2.0}_{-0.4}$ km. The basin center has been partially resurfaced by Mare Orientale, a low albedo thin volcanic deposit formed after the basin (Fig. 1b) (Head, 1974; Whitten et al., 2011). Smaller mare ponds are found in isolated locations interior to the Inner Rook and Outer Rook rings, revealing minor post-impact volcanic modification of the ring structures. In Bouguer gravity data (Fig. 1c), the basin is characterized by a strong positive central anomaly marking the uplifted mantle plug (Neumann et al., 2015b, 1996; Wieczorek and Phillips, 1999; Zuber et al., 2016), surrounded by a negative annulus (Andrews-Hanna, 2013; Wieczorek and Phillips, 1999; Zuber et al., 1994) due in part to the

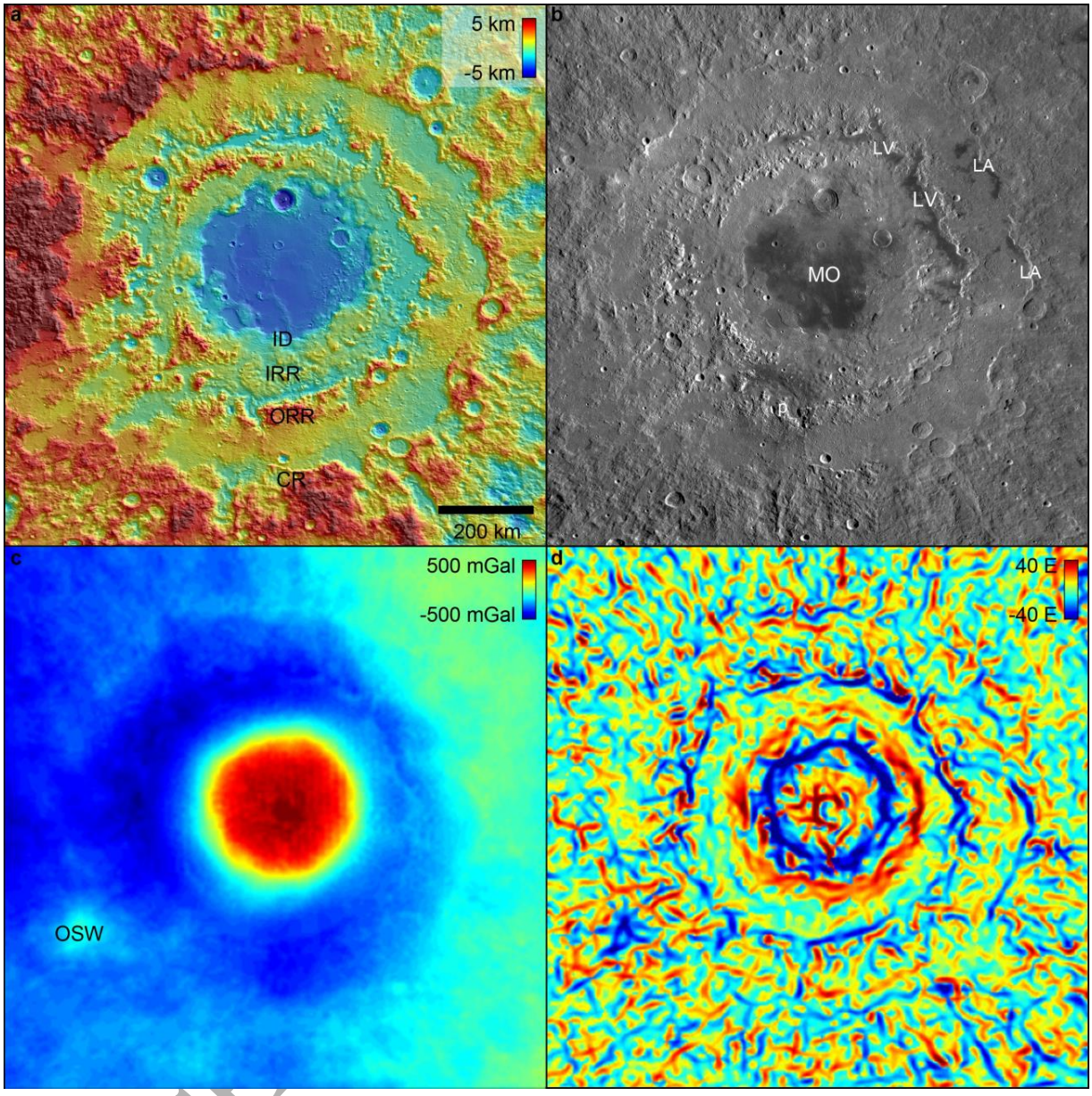

Figure 1. The Orientale basin as seen in **a** topography, **b** WAC image mosaic, **c** Bouguer gravity, and **d** Bouguer gravity gradients (in Eötvös, where 1 *E* is 10^{-9} s^{-2}). The edge of the inner depression (ID), Inner Rook ring (IRR), Outer Rook ring (ORR), and Cordillera ring (CR) are labeled in **a**. Mare deposits associated with Mare Orientale (MO), Lacus Veris (LV), and Lacus Autumni (LA), and a dark pyroclastic ring deposit (p) are labeled in **b**. The pre-existing Orientale Southwest (OSW) basin is marked in c. Maps are in cylindrical projection spanning 40° of latitude and longitude, centered on 20°S 266°E (see box in Fig. 2).

thickening of the crust by ejecta (Fassett et al., 2011; Head, 1974). The positive center and negative annulus are both found in the free air gravity as well, indicating the presence of a sub-isostatic annulus that drove uplift of the super-isostatic center (Andrews-Hanna, 2013; Freed et al., 2014; Melosh et al., 2013).

The subsurface structure of the basin is critical for understanding the formation of the basin and its rings. The appearance and topography of the ring scarps of Orientale supports the interpretation of faults at the Outer Rook and Cordillera rings (Hartmann and Kuiper, 1962; Head, 1974), but the associated subsurface structure implied by the topography can only be inferred by comparison to mechanical models (Nahm et al., 2013). Gravity data provide more direct constraints on the subsurface structure, but early studies of lunar crustal structure could not fully resolve the rings due to the low resolution and variable quality of pre-GRAIL data (Neumann et al., 1996; Wieczorek and Phillips, 1999). Inversions of pre-GRAIL gravity data that had been azimuthally averaged around the basin found evidence for a fault beneath the Cordillera ring, but were unable to determine if a similar fault exists beneath the Outer Rook and/or if the faults extend down to the crust-mantle interface (Kattoum and Andrews-Hanna, 2013). Azimuthally averaged crustal thickness models from pre-GRAIL data found suggestions of ring faults reaching the crust-mantle interface at both the Outer Rook and Cordillera (Andrews-Hanna, 2013), but were limited in resolution and could not reveal the 3D structure of the basin. In addition, the larger errors and variable spatial resolution of pre-GRAIL gravity at relevant wavelengths make interpretations of the ring structures difficult. High-resolution gravity data from GRAIL (Zuber et al., 2013a, b) were used to generate crustal thickness profiles averaged over 30° of azimuth (Zuber et al., 2016), revealing large (~20 km) undulations in the relief along the crust-mantle interface interpreted as ring faults crossing and offsetting that

interface. However, the rings are difficult to discern in map-view in most high-resolution crustal thickness models, requiring new methodologies and analyses.

In this study, we use high-resolution gravity data from NASA's GRAIL mission (Zuber et al., 2013a,b) together with new modeling techniques in order to constrain both the shallow and deep structures associated with the Orientale basin rings. For shallow structures, we use the second horizontal derivatives of the high-pass filtered Bouguer gravity potential, hereafter referred to as the gravity gradients (Andrews-Hanna et al., 2013a). In order to probe the deep structure of the basin, we use a novel approach to invert the gravity data for the relief along the crust-mantle interface in order to look for evidence of ring-faults extending to the base of the crust. The results of these analyses show evidence for ring faults and ring dikes cutting through the crust, placing quantitative constraints on the fault dips, dike dimensions, and other aspects of the basin structure.

2. Methods

This analysis of the subsurface structure of Orientale included calculation of gravity gradients, inversion of gravity gradients for the properties of the underlying dikes or faults, and models of the crustal structure of the basin and its system of rings. The methodology is described briefly below, and full details are included in the Appendix and associated references. All analyses used the JGGRX_1500E gravity model, with a half-wavelength resolution of 3.6 km at degree 1500 (Konopliv et al., 2014; degree 1500 model is available on the PDS).

2.1. Gravity gradients

The majority (~98%) of the short wavelength free-air gravity field of the Moon is dominated by the effects of topography (Zuber et al., 2013b). When the effects of topography are removed to generate a Bouguer gravity map, the remaining short wavelength signal arising in the subsurface is much smaller in magnitude than the larger scale anomalies. The short wavelength Bouguer gravity anomalies are best highlighted using the gravity gradients, calculated as the maximum amplitude eigenvalues of the second horizontal derivatives of the high-pass filtered Bouguer gravity potential (Andrews-Hanna et al., 2014; Andrews-Hanna et al., 2013a). The short wavelength Bouguer gravity gradients are dominated by the effects of shallow structures, since short wavelength anomalies arising from greater depths within the crust are strongly attenuated at the surface.

The Bouguer gravity was calculated using the spatially variable crustal density determined from the GRAIL data (Wieczorek et al., 2013). The Bouguer gravity gradients were then calculated using the methodology of Andrews-Hanna et al. (2013a), with a high pass filter centered at degree 50 and a low-pass filter centered at degree 500 (half-wavelength resolutions of 110 km and 11 km, respectively). However, the gravity gradients are strongly sensitive to the elevation of the reference surface relative to the source of the anomalies. At these high degrees, the effect of the variable elevation of the lunar surface results in prominent differences in the magnitude of the nearside and farside gravity gradients. To avoid these artificial variations in the magnitudes of the gradients, we calculated the gravity gradients on a smooth (spherical harmonic degree 50) representation of the surface topography rather than on a sphere (Fig 2; see Appendix A1). Calculating the gravity gradients on the smoothed topography as a reference surface is critical for both qualitative and quantitative comparisons of the gravity gradients in areas of different mean topography, such as the eastern and western portions of the Oriental basin rings.

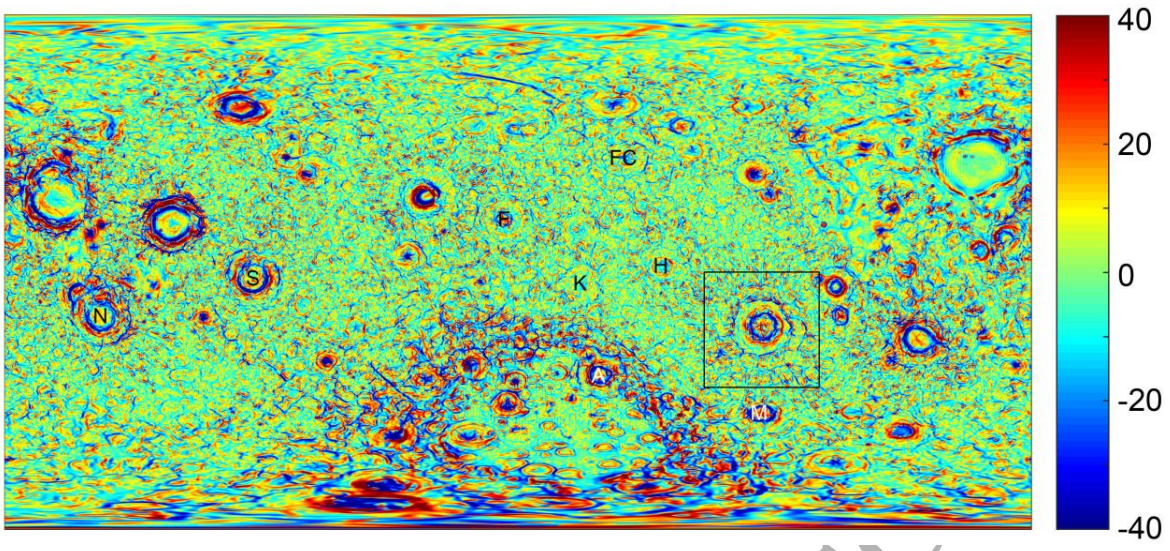

Figure 2. Global gravity gradient map (in Eötvös) calculated on a smooth degree 50 model of the topography. The location of the maps in Fig. 1 are shown by the black box. Map is in a cylindrical projection centered on the lunar farside. Basins mentioned in the text are labeled, including Korolev (K), Nectaris (N), Fowler-Charlier (FC), Smythii (S), Apollo (A), Hertzsprung (H), Freundlich-Sharonov (F), and Mendel-Rydberg (M).

2.2. Gravity gradient profiles

Visual inspection of the gravity gradients of the Orientale region reveals concentric quasi-circular structures associated with the continuation of the basin rings into the subsurface (Fig. 1d). However, the random background variations in the gravity gradients are of comparable magnitude to the signal of interest at the rings. These background variations are not noise in the data, but instead reveal seemingly random, small-scale density anomalies within the upper crust (Jansen et al., 2017). This variability poses a challenge to any study of small-scale (<100 km) subsurface structures using the GRAIL data. In order to reveal the structure of the rings, it is desirable to average multiple ring profiles in order to preserve coherent patterns associated with the rings while reducing the background variability. However, asymmetries in the basin structure do not allow simple averaging of profiles. Individual radial profiles of the gravity gradients were stretched in the horizontal direction using linear stretching functions to

align the basin rings in different profiles and then averaged (see Appendix A2). The resulting averaged profile shows low amplitude gravity gradients away from the basin rings and large amplitude gradients at the basin rings (Fig. 3), and thus has isolated the ring signatures from the background variability.

In interpreting the gravity gradients, a negative gravity gradient indicates a negative concavity in the potential as would occur above either a positive line mass or point mass anomaly. A positive gravity gradient indicates a positive concavity in the potential as would occur above a negative line mass or point mass anomaly. A symmetric pair of positive and negative gradients is predicted at the edge of a finite plane of anomalous mass. Thus, a negative gravity gradient along a linear or arcuate trend is most simply explained by the presence of a narrow subsurface dike of greater density than its surroundings (Andrews-Hanna et al., 2013a). A symmetric pair of positive and negative gravity gradients is most simply explained by a layer of anomalous density that has been offset across a fault. At larger scales, a pair of positive and negative gravity gradients is expected at the edge of the uplifted mantle plug in the center of the basin.

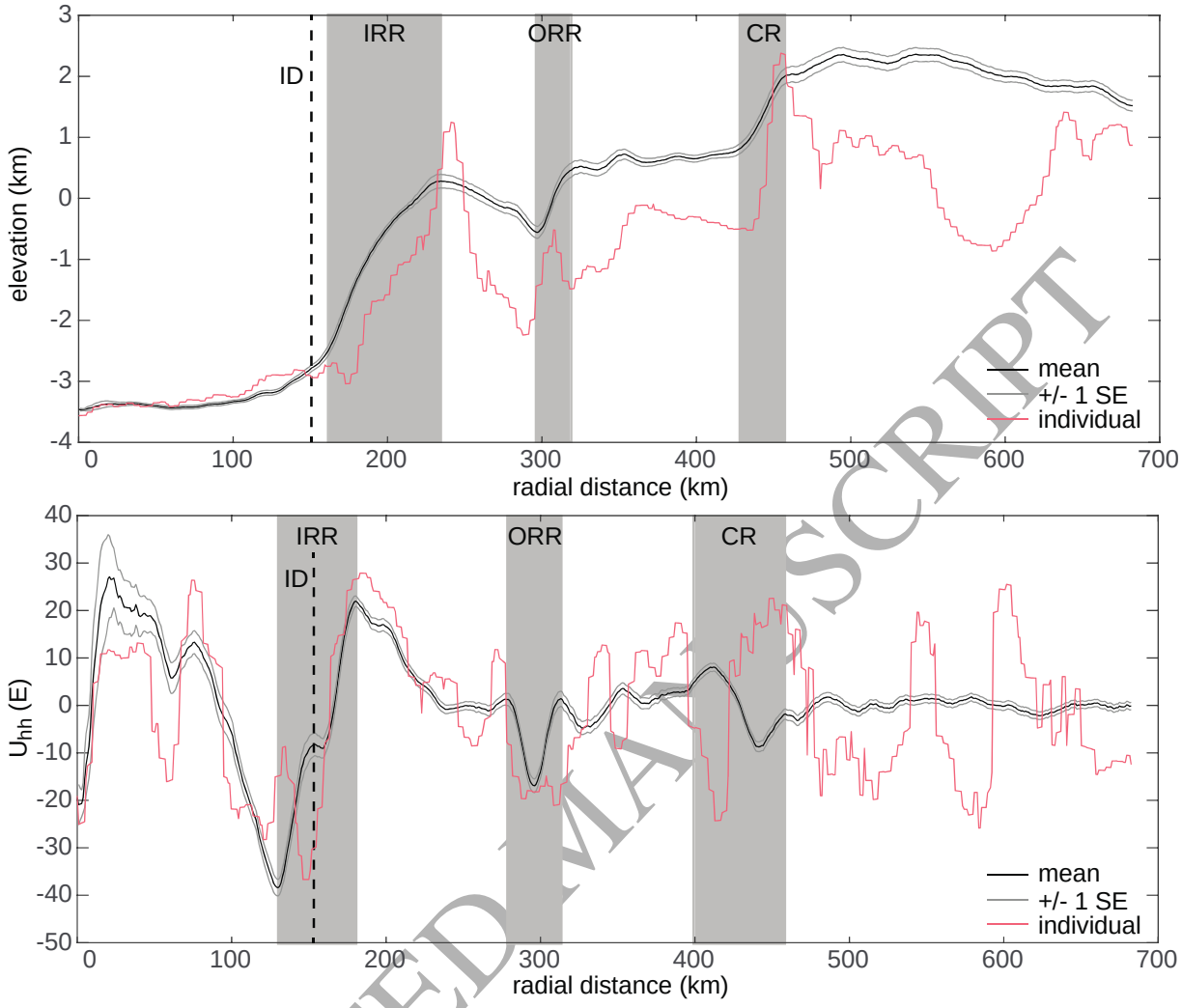

Figure 3. Average of the aligned radial profiles of the topography (top) and gravity gradients (bottom), showing the mean and ±1 standard error profiles, generated between azimuths of 90 and 360° (clockwise from north). For comparison, randomly chosen individual profiles of the topography and gravity gradients are included (red line). The locations of the transitions in topography and gravity gradient for the Inner Rook ring (IRR), Outer Rook ring (ORR), and Cordillera ring (CR) are highlighted by the gray boxes. The location of the edge of the inner depression (ID) is marked with a dashed line.

2.3. Gravity gradient inversions

Isolated sections of the average gravity gradient profiles corresponding to the Outer Rook and Cordillera rings were chosen for inversion for the associated subsurface structure (dike or fault offset). The gravity gradients were chosen for the inversion rather than the simple Bouguer gravity because the small structures of interest produce very subtle signatures in the Bouguer

gravity relative to the large amplitude long wavelength anomalies associated with the basin itself, but they produce dramatic signatures in the gravity gradients (Fig. 1c,d).

The inversion used a Monte Carlo model together with forward models of the gravity gradients arising from simple geometric structures in order to identify the optimal model parameters and their associated uncertainties (Andrews-Hanna et al., 2013a; Metropolis et al., 1953; see Appendix A3). The inversions focused on isolated sections of the observed gravity gradient profile, and were set up to represent structures as either dikes or faults, based on a qualitative interpretation of the data as discussed above.

Ring dikes were represented as rectangular prisms (Fig. 4) with an assumed density contrast of 500 kg/m^3, consistent with the density contrast between the lunar upper crust of ~2550 kg/m^3 (Wieczorek et al., 2013) and measured bulk densities of Apollo samples of lunar basalts of ~3010-3247 kg/m^3 (Kiefer et al., 2012). In the Monte Carlo model, the width, top depth, and dip of the dikes were left as free parameters. Because of vertical attenuation, the solutions are only weakly sensitive to the assumed bottom depth, and models in which the bottom depth was left unconstrained resulted in nearly identical minimum RMS misfits for bottom depths greater than ~10 km. For dikes rising from deep in the mantle to the level of neutral buoyancy, it is expected that the dikes will extend across the crust-mantle boundary into the overlying crust (Head and Wilson, 2017; Wilson and Head, 1981), so we fix the effective bottom depth as seen by the gravity data at the approximate depth of the crust-mantle interface of ~50 km. Because the preferred dike widths are narrower than the resolution of the data, the width of the best-fit dike will scale simply with the inverse of the density contrast, so the effects of larger or smaller density contrasts can easily be accounted for.

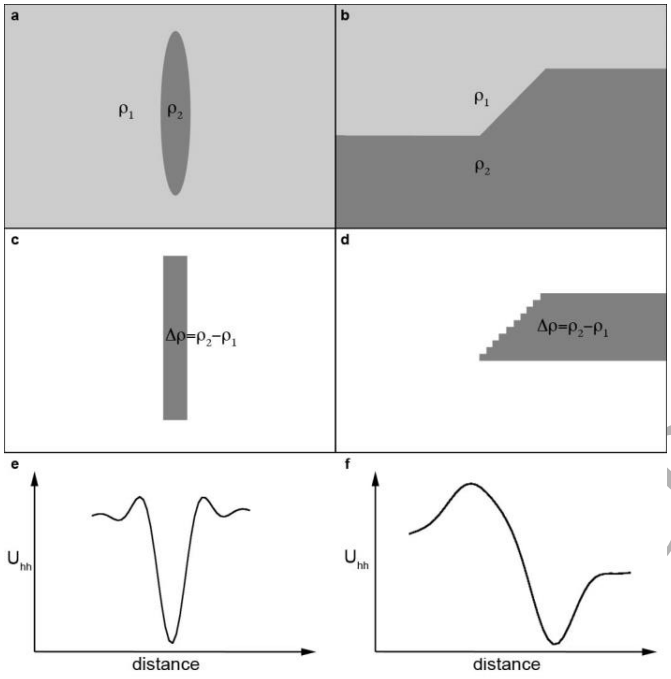

Figure 4. Schematic representation of the gravity gradient models. Cartoon representations of a dike (**a**) and fault offset of a subsurface interface (**b**) are represented in the inversion model using rectangular elements (**c,d**), leading to characteristic gravity gradient signatures (**e,f**).

Discrete density anomalies could also arise from a fault offset across a shallow subsurface density interface, which would generate a step across that interface. Such an interface could arise in a layered density structure associated with lava flows on the surface, sills at depth, compositional stratification of the crust, a megaregolith layer, or basin ejecta. For the purposes of a gravity inversion, the fault can be represented as a sloping offset across a density interface bounding the top of a semi-infinite half-space (Fig. 4). The horizontally uniform densities above and below this step have no impact on the gravity gradients and are not included in the model. The sloping step itself was represented using 10 rectangular prisms in a stair-step pattern on the footwall side of the fault, extending from the interface depth in the footwall to the interface depth in the hanging wall, with a density contrast equal to that across the interface. The vertical dimension of the step (the fault offset) was set equal to the inferred fault offset of ~4 km based

on the surface scarp (Nahm et al., 2013), and the dip, depth and density contrast were left as free parameters. The gravity gradients arising from the corresponding steps across the base of the crust are strongly attenuated at the surface at higher degrees, and are neglected in this inversion. The expression of the ring faults at the crust-mantle interface is instead examined using crustal thickness models, as described below.

2.4. Crustal thickness modeling

To examine the deeper structure of the basin, we generated models of the crustal thickness using a modified version of the model of Wieczorek and Phillips (1998). Global crustal thickness models are limited by the pervasive small-scale gravity anomalies which arise from shallow density anomalies in the crust (Jansen et al., 2017). During the downward continuation of the Bouguer gravity to the depth of the crust-mantle interface (e.g., Wieczorek, 2007), shorter wavelengths (higher degrees) are amplified more than longer wavelengths (lower degrees), and the small-scale gravity anomalies arising from shallow density anomalies are unstably amplified. GRAIL-derived global crustal thickness models (Wieczorek et al., 2013) excluded these small-scale anomalies by filtering the gravity data to a uniform resolution of ~68 km (the half-wavelength resolution at degree 80, at which the filter amplitude dropped below 0.5). The resulting models have higher resolution than pre-GRAIL models with filter magnitudes of 0.5 at degrees 30 (Wieczorek and Phillips, 1998; Wieczorek, 2006) and 50 (Ishihara et al., 2009). However, this limiting resolution nevertheless resulted in loss of signal from the crust-mantle interface at shorter wavelengths. Maps of the residual gravity anomaly not included in the GRAIL global crustal thickness models show anomalies in the range of ±40 mGal in the vicinity of the major basins (e.g., Figure 1b of Jansen et al., 2017). As a lower

bound, this equates to ±1.4 km of un-modeled relief along the crust-mantle interface, based on an infinite slab approximation with crust and mantle densities of 2550 and 3220 kg/m^3, respectively. Given the degree-dependent attenuation of the gravity anomalies at the surface and the scale of the structures of interest, the actual un-modeled relief along the crust-mantle interface is likely much larger. Other studies have used azimuthal averaging to attempt to resolve ring structures (Andrews-Hanna, 2013; Kattoum and Andrews-Hanna, 2013; Zuber et al., 2016), but were not able to resolve the subsurface structure of the rings in map view or the variations in their properties with azimuth.

To avoid instabilities in models of the crust-mantle interface relief, some filtering is required to suppress small-scale gravity anomalies arising from shallow density anomalies. We used a novel approach with spherical harmonic filters that take advantage of the natural radial symmetry of the basin. By filtering the data more strongly in the azimuthal direction than in the radial direction, small-scale gravity anomalies that are uncorrelated with the basin structure can be minimized while preserving the small-scale gravity anomalies that are related to the basin rings. This results in a crustal thickness model that has higher resolution in the radial direction than in the azimuthal direction, thereby enabling it to better resolve the structure perpendicular to the rings. Our approach entailed rotating the basin to the pole and using a degree- and order-dependent filter, resulting in an azimuthal resolution of 121-182 km and radial resolution of 34-39 km (see Appendix A4). This model provides nearly a factor of 2 better resolution in the radial direction than the globally stable uniform resolution models of Wieczorek et al. (2013), and easily resolves the structures of the Outer Rook and Cordillera rings with their typical spacing of 100-120 km.

Interpretations of GRAIL gravity data have shown that the upper crust has a higher porosity than was previously assumed (Wieczorek et al., 2013), with an average upper crustal porosity of ~12%, and an annulus around Orientale with a porosity of ~17% representing the ejecta blanket of that basin. Both of these values are in keeping with the measured porosities of lunar samples (Kiefer et al., 2012). However, subsequent GRAIL analyses have shown that the best-fit density and porosity is a function of wavelength, consistent with a density that increases with depth, with an average farside density gradient of 35 kg/m^3/km (Besserer et al., 2014). This density gradient may reflect the effects of both the decreasing porosity with increasing pressure and temperature, as well as a possible increase in the mafic mineral content of the lower crust.

A crustal thickness model that neglects the increase in density with depth within the crust may over-estimate the amplitude of the undulations along the crust-mantle interface, since the gravity anomalies are amplified more during downward continuation to the crust-mantle interface than during downward continuation to density transitions at intermediate depths within the crust. Although two-layer crustal thickness models are fundamentally under-constrained, such models can be generated by making assumptions regarding the behavior of the density interfaces (e.g., Wieczorek and Phillips, 1998). We have generated both uniform and two-layer crust models of Orientale.

We made the simple assumption of a two-layer crust (representing a feldspathic upper crust and mafic lower crust, or a high porosity upper crust and a low porosity lower crust) in which the intra-crustal density interface lies approximately in the middle of the crust, and the density jumps across both the intra-crustal interface and the crust-mantle interface are approximately equal (Andrews-Hanna, 2013). We adopt an upper crust density of 2400 kg/m^3 representative of the surface density around Orientale, a mantle density of 3220 kg/m^3

(Wieczorek et al., 2013), and a lower crust density of 2800 kg/m^3. The intra-crustal interface was assumed to lie parallel to the crust-mantle interface, as would be expected when deformation associated with an impact basin and its rings displaces the entire crustal column. However, the intra-crustal interface was not allowed to rise above the surface. Around Orientale, these assumptions result in a model consistent with thickening of only the upper crust within the ejecta blanket, excavation of the entire upper crust and a portion of the lower crust within the central cavity, and deflections associated with the ring faults along the intra-crustal interface and crust-mantle interface that are equal in amplitude.

Average profiles were constructed across sectors with similar structure as revealed in contour maps of the relief along the interfaces. From these profiles, the locations where faults cross the interfaces were chosen at the inflection points between an inner upward concavity and outer downward concavity, based on the expected expression of a filtered step function. One limitation of the layered crust models is that the intra-crustal interface and crust-mantle interface are constrained to be parallel, effectively imposing vertical faults in the lower crust. However, at the limit of the crustal thickness model resolution, the gravity anomalies arising from the intra-crustal interface at a depth of 25 km are ~10× greater in amplitude than those arising from the crust-mantle interface at a depth of 50 km when both are measured at the surface, or 3× greater at the wavelength corresponding to the spacing between the Inner and Outer Rook. Thus, the gravitational signature of the ring faults is dominated by the relief along the intracrustal density interface, and the dip angles for the layered crust models were calculated between that interface and the surface. Because the radial position of the inflection along the intra-crustal interface in the layered crust model is generally the same as the inflection along the crust-mantle interface in

the uniform crust model, dip angles for the layered crust models are lower than for the uniform crust models.

3. Results and interpretation

3.1. Gravity gradients

In map view and in profile, the gravity gradients show strong anomalies associated with the basin rings. However, the background variability seen both in map view and in one randomly chosen radial profile of the gravity gradients is of the same magnitude as the prominent anomalies associated with the ring structures (Figs. 1d, 3b). The signature of the rings only becomes clear in the averaged profiles. The full radial profile in Fig. 3 is averaged between azimuths of 90° and 360° (clockwise from north; excluding profiles containing a small pre-Orientale basin at an azimuth of 240°) as these azimuths show similar characteristics in the gravity gradients.

Inner Rook Ring. The prominent negative gravity gradient at a radial distance of ~130 km from the basin center coincides with the outer edge of the uplifted mantle plug at the transition from the thin crust below the basin floor to the wall of the excavated cavity (see crustal thickness models in Section 3.2). The negative gravity gradient indicates a downward concavity in both the gravity and the crust-mantle interface. The strong positive gravity gradient anomaly at ~190 km radius is associated with the outer edge of the uplifted mantle plug at the transition from the wall of the excavated cavity to the surrounding thicker crust, and occurs at a point where the crustal thickness is close to the pre-impact value taken from beyond the ejecta blanket of the basin (see Section 3.2).

The relatively large amplitude of this pair of gravity gradient anomalies is consistent with the relatively large amplitude in the topographic relief across the Inner Rook ring, which is the most prominent topographic ring bounding the central zone of excavated crust. We interpret this pair of anomalies to be the equivalent of the Inner Rook ring expressed at the crust-mantle interface. Thus, the location of the positive gravity gradient anomaly in this pair provides the best measurement of the radius of the excavated crustal cavity of ~190 km (c.f., Johnson et al., 2016). However, as previously noted by Zuber et al. (2016), this radius is less than the 232-km radius of the Inner Rook ring. This offset between the expression of the edge of the excavated crustal cavity seen at the crust-mantle interface and the edge of the central topographic cavity at the Inner Rook is also seen in the crustal thickness models, but at lower resolution than can be obtained with the gravity gradients (see Section 3.2). This offset is consistent with the predicted inward translation of deep material towards the basin center during the collapse of the transient cavity (Johnson et al., 2016; Melosh and Mckinnon, 1978; Potter, 2015). The positive gravity gradient lies interior to the radius of maximum crustal thickness, possibly reflecting the separation between the edge of the cavity of excavated crust and the maximum crustal thickening by the ejecta of the basin.

Inner depression. Between the negative and positive gradient anomalies in the pair described above, a subtle positive inflection in the gravity gradient profile at a radius of ~150 km is aligned with the topographic bench that marks the edge of the inner depression. The inner depression has been interpreted as having formed through the thermal contraction of the solidified melt pond contained within the basin (Head, 1974; Vaughan et al., 2013). However, the composition of the upper crust within the inner depression may be more compatible with a thin homogenous melt sheet (Spudis et al., 2014) or may instead support a thin layer of crustal

material having flowed over the basin center during the collapse of the transient cavity (Johnson et al., 2016). Remote sensing constraints on the melt sheet's composition, combined with measured bulk densities of Apollo impact melt breccias, show that the solidified melt pond should have a greater density than the surrounding crust (Zuber et al., 2016). The higher density melt pond, whether exposed at the surface or buried beneath a crustal cap, would result in a pair of negative and positive (inner and outer) gravity gradients flanking the edge of the melt pond. However, because the melt pond lies within the depression associated with the central crustal cavity, the signature of the melt sheet is superimposed on the much larger signature of the edge of the uplifted mantle plug. The observed gravity gradient profile is consistent with an interpretation in which the positive anomaly associated with the edge of the melt sheet is expressed as a small inflection within the larger Inner Rook gravity gradient pair, and the negative anomaly associated with the melt sheet aligns with and adds to the negative anomaly from the uplifted mantle plug. This is supported by the larger magnitude of the negative Inner Rook anomaly (-38 E) in comparison with the positive Inner Rook anomaly (+22 E). Due to the superposition of the inner depression edge and Inner Rook anomalies, we have not attempted quantitative inversion of these anomalies.

Outer Rook Ring. A discrete negative gravity gradient anomaly at a radius of 290 km lies just interior to the Outer Rook ring. The negative gravity gradient indicates a subsurface mass excess (Andrews-Hanna et al., 2013a), which is most simply explained by a dense igneous intrusion along the ring fault. This interpretation is consistent with the presence of mare basalt ponded within the Outer Rook ring in the northeastern quadrant of the basin in Lacus Veris (Fig. 1b; Head, 1974; Whitten et al., 2011), and a local pyroclastic deposit centered on the ring in the southwestern quadrant of the basin (Fig. 1b; Head et al., 2002). Despite the localized nature of

these surface deposits, the gravity gradients indicate that the intrusion into the ring fault fully encircles the basin. The existence of a continuous circumferential ring dike revealed by gravity but only discontinuous surface eruptions concentrated in the northeast is consistent with the effect of the regional gradient in crustal thickness that favors eruptions in regions of thinner crust as a result of buoyancy effects (Head and Wilson, 2017; see also Nahm et al., 2013).

As with all analyses of potential field data, our interpretation of a ring dike is not unique. An alternative interpretation of this Outer Rook gravity gradient is that it is the result of low porosity and thus high density impact melt ponded within the ring structure on the surface. This interpretation is supported by the fact that some of the negative gravity gradients are aligned with smooth non-mare material within the depressions adjacent to the Outer Rook, though in other places the negative gravity gradient ring occurs in rough high-standing material. However, this interpretation is at odds with the corrugated and fractured appearance of the Orientale melt in the Maunder formation that is suggestive of a high porosity (Head, 1974), and the measured high porosity of lunar impact melt breccias (Kiefer et al., 2012). Melted mantle material that has been predicted to splash out over the surface during the impact could provide a greater density contrast (Johnson et al., 2016), but has not been identified in remote sensing data. Moreover, some basins lack similar negative gravity gradient anomalies associated with some or all of their ring structures, though the amount and distribution of impact melt may vary depending on the velocity and angle of the impact. Nevertheless, it is possible that impact-melted crust or mantle material ponded within the ring fault depression could contribute to the gravity anomalies. Additional work is also needed to examine the possibility that the alignment of separate structures at shallow and deep levels within the crust could mimic the signature of a ring dike. Despite these uncertainties, both the gravity gradients and the geological evidence in the form of

mare and pyroclastic deposits support our interpretation of a ring dike intruded into the Outer Rook fault.

Dikes have been found to follow pre-existing faults on both Earth (Gaffney et al., 2007) and Mars (Cole and Andrews-Hanna, 2017). Generally, faults must be within 45° of the preferred angle for dike intrusion in order for the fault capture the dike (Gaffney et al., 2007), though on Mars there is evidence for capture of a dike or sill by a low angle thrust fault (Cole and Andrews-Hanna, 2017). The stresses associated with the central load or mass concentration (mascon) may also play a role in controlling intrusive activity (McGovern et al., 2014).

The symmetric signature of the Outer Rook gravity gradients between azimuths of 90° and 360° (measured clockwise from north) is indicative of a nearly vertical ring dike. The Monte Carlo inversion of this profile yields a dike with a width of 1.4 km (1.0-2.1 km, 1-σ range) and a dip of 96° (74-117°), extending between a top depth of 3.8 km (1.9-6.9 km) and the assumed bottom depth at the base of the crust of 50 km (Fig. 5a-d). The preferred dip is indistinguishable from vertical. Although these results are permissive of dikes dipping away from the center of the basin (dips >90°), an outward dipping fault at the Outer Rook is unlikely given the topography. The asymmetric signature of the Outer Rook gravity gradients in the northeastern quadrant (azimuths of 45-90°), with a small positive anomaly exterior to the larger negative anomaly, indicates an inward dipping ring dike (Fig. 5e-h). A Monte Carlo inversion for the best-fit ring dike properties supports a dike with a width of 5.7 km (4.8-16.5 km, 1-σ range) and a dip of 47° (33-77°), extending between a top depth of 13 km (9-24 km) and the assumed bottom depth at the base of the crust of 50 km. We cannot rule out the possibility that the surface mare deposits in this quadrant affect the gravity signature, since mare ponded above the sloping hanging wall block (Nahm et al., 2013) would also have an asymmetric gravity

signature, though our interpretation of a lower dip angle in this quadrant is corroborated by the results of the crustal thickness models in the next section. The best-fit dike widths from these inversions scale with the inverse of the density contrast, assumed to be 500 kg/m^3 here. Density contrasts up to 700 kg/m^3 (Kiefer et al., 2012) would reduce the widths by up to 30%. We note that these widths are much larger than typical dikes observed on Earth, and are more similar to the randomly oriented ancient igneous intrusions revealed by previous analyses of GRAIL data (Andrews-Hanna et al., 2013a).

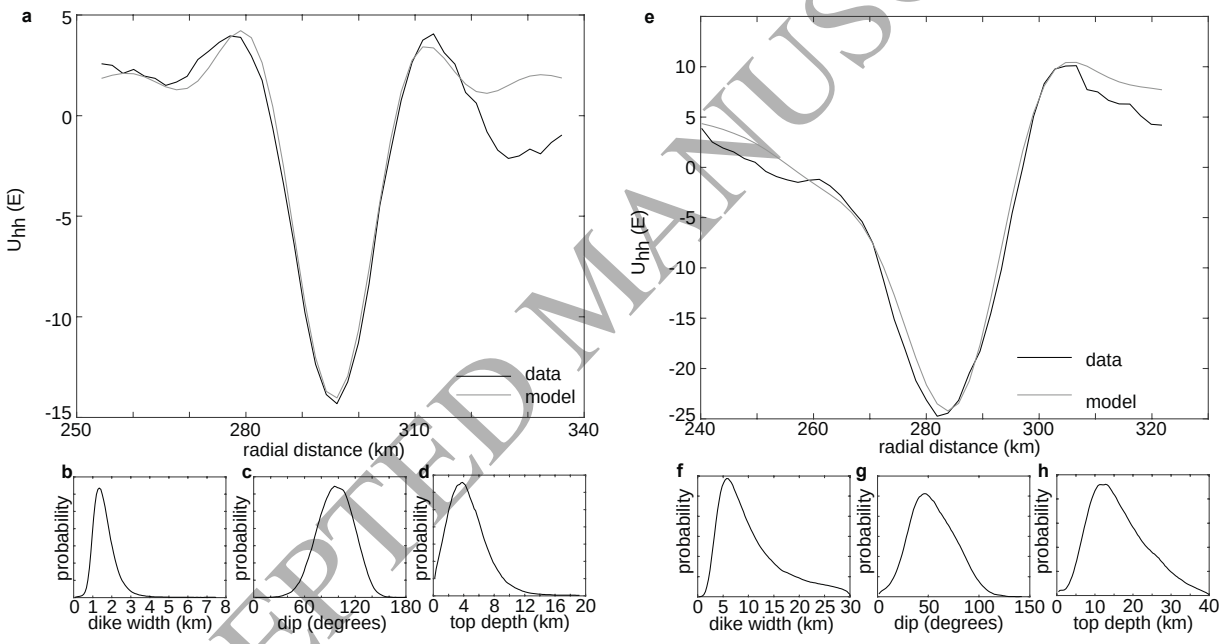

Figure 5. Gravity gradients and inversion results for the Outer Rook. **a** Average gravity gradient profile of the Outer Rook between azimuths of 90° and 360°, compared with the best-fit model from the inversion. **b-d** Normalized probability density functions for the dike width, dip, and top depth for the profile in **a**. **e-h** Same as **a-d** but for azimuths of 45° to 90°.

The dimensions of this ring dike leads to a total intrusive volume within the crust of 2.4×10^5 km^3 (1.8-4.1 $\times10^5$ km^3, 1-σ range), which is ~20× greater than the estimated volume of Mare Orientale within the basin center of 1.0×10^4 km^3 (based on a mare thickness of <0.2 km

and area of 5.2×10^4 km^2; Head, 1974; Whitten et al., 2011), 84× greater than the minimum volume of the mare ponded within the rings (Whitten et al., 2011), and 18× greater than the volume of all mare deposits associated with the basin (Whitten et al., 2011), revealing the important contribution of subsurface intrusions to the magmatic evolution of the basin. The high ratio of intrusive to extrusive material has parallels in the smaller floor fractured craters that are common on the Moon (Jozwiak et al., 2017, 2015; Thorey et al., 2015). We note that the gravity anomaly in the northeast quadrant of the Outer Rook likely includes some contribution from the extrusive Lacus Veris mare. If we instead assume that the dike dimensions from the rest of the basin are representative of this quadrant as well, we obtain an intrusive volume of 1.2×10^5 km^3 ($1.0\text{-}1.8\times10^5$ km^3), which still greatly exceeds the estimated volume of extrusive material in Mare Orientale. These volumes are only representative of that portion of the dike within the crust, since the dike within the mantle contributes little to the gravity at the surface due to its low density contrast and great depth.

Cordillera ring. The majority of the Cordillera ring does not show an obvious dike signature in the gravity gradients, and is instead characterized by a symmetric pair of positive and negative gravity gradient anomalies (Fig. 6). This signature is consistent with an offset along a fault across an interface separating a lower density upper layer from the underlying higher density crust. We inverted the gravity gradients assuming a 4-km step across a subsurface density interface, based on the topographic expression of the ring (Nahm et al., 2013), using a Monte Carlo model to constrain the depth of the offset interface on the outer side of the step, the density contrast, and the dip of the offset. Unlike the inversions of the Outer Rook dike, the results of the Monte Carlo model for the Cordillera fault permit a wide range of parameter space, with a best-fit model that lies outside of the 1-σ range of the most probable models. The most

probable model has a density interface at a depth of 11 km (7-20 km, 1-σ range) with a density contrast of 300 kg/m^3 (230-510 kg/m^3) and a dip that is effectively unconstrained. The best-fit model has a density interface at a depth of 0.5 km with a density contrast of 200 kg/m^3 and a dip of 8°. The difference between the best-fit and most probable models reveals that the depth of the interface is poorly constrained. A continuous variation in density over this range of depths may be expected to yield similar results. Although the inversion does not place useful constraints on the fault dip, the center of the gravity gradient signature is shifted toward the basin center by ~15 km relative to the center of the topographic scarp of the Cordillera, supporting an inward dipping fault. For the range of depths favored by the inversion, this leads to dips of 25-54°. However, given the uncertainty in the depth to the top of the density interface, this dip estimate may not be reliable.

Although a wide range of models provide acceptable fits to the Cordillera, these results are consistent with the subsurface density interface representing the contact between the low density Orientale ejecta (~2400 kg/m^3) and the mean crustal density of 2550 kg/m^3 (Wieczorek et al., 2013), at the base of a 3 km-thick ejecta blanket (Fassett et al., 2011). The expected density contrast and thickness for the ejecta blanket lie in between the best-fit and most probable models. This interpretation is consistent with the fact that Orientale, as the youngest large basin, is one of the few basins surrounded by a prominent low-density ejecta blanket (Wieczorek et al., 2013), and the paired gravity gradient signature at the Cordillera is similarly rare among lunar basin rings. However, given the range of acceptable solutions, other interpretations of the shallow crustal structure at this location are possible, such as an offset across the base of a discrete megaregolith layer at a deeper level within the upper crust. This fault signature may not be apparent at the Outer Rook due to the greater thickness of the ejecta there (and thus greater

attenuation of anomalies arising at the base of the ejecta sheet), as well as the effect of the greater magnitude of the ring dike anomalies.

Between azimuths of 83° and 125°, the gravity gradient signature of the Cordillera is characterized by a weak positive anomaly interior to a more prominent asymmetric negative anomaly (Fig. 6e). This signature is consistent with the superposition of anomalies arising from a ring dike and ring fault. Alternatively, these anomalies could indicate an outward dipping ring dike, though this is interpretation is deemed unlikely as it is at odds with the inward dipping fault indicated by the crustal thickness models below. This region is characterized by only a few small mare deposits at the northern end of the dike-like gravity anomaly, whereas a weaker ring dike gravity signature is associated with the larger Lacus Autumni mare ponded within this ring further to the north, indicating that the dike rather than the mare dominates the gravity gradient signature. However, due to the ambiguity in the interpretation of the gravity gradients, the possible contribution of surface maria to the gravity, and the greater non-uniqueness expected in the inversion arising from the combination of dike and fault signatures, we have not attempted an inversion of this anomaly.

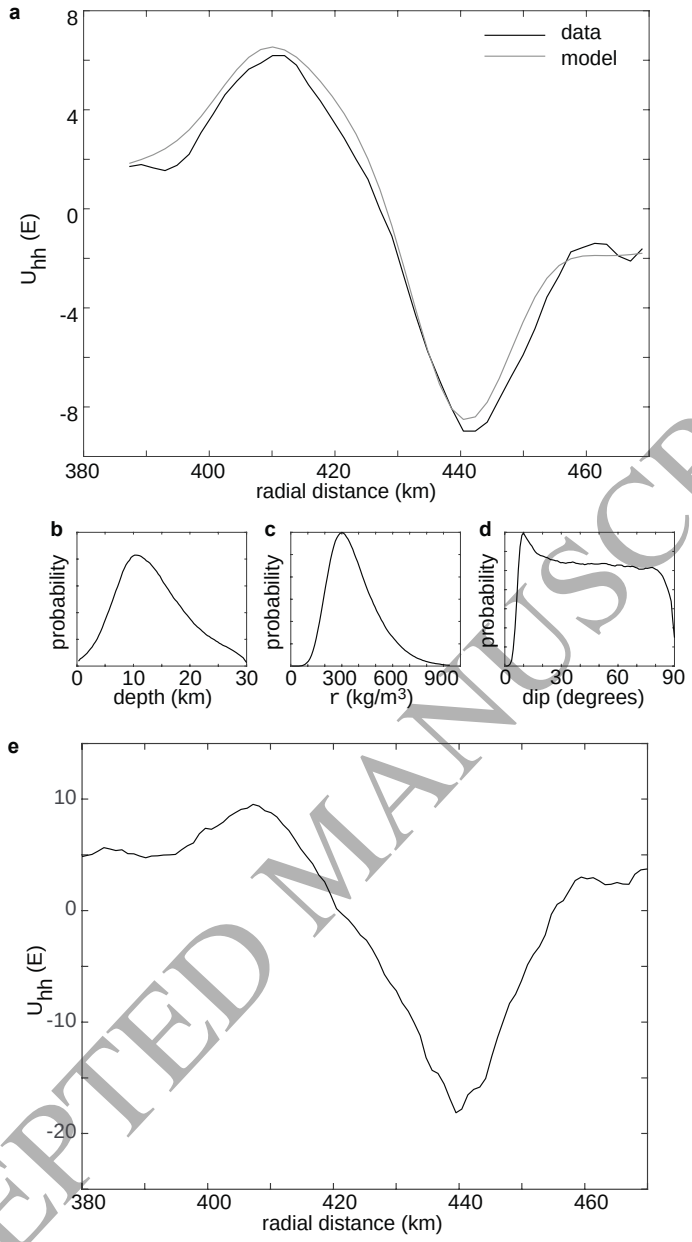

Figure 6. Gravity gradients and inversion results for the Cordillera. **a** Average gravity gradient profile of the Cordillera between azimuths 130° to 215° and 250° to 83° (avoiding a segment with a dike-like signature to the east and a pre-existing basin to the southwest), compared with the best-fit model from the inversion. **b-d** Normalized probability density functions for the depth to the offset interface, the density contrast across that interface, and the fault dip for the profile in **a**. **e** Average gravity gradient profile of the Cordillera between azimuths of 83° and 125°.

3.2. Crustal structure of Orientale

We first constructed a crustal thickness model using a simple degree-dependent filter with a uniform resolution comparable to the radial resolution of our degree- and order-dependent filters (Fig. 7c). This model applied a cosine taper between degrees 130 and 150, as a model tapered between degrees 140 and 160 (the radial resolution of our other models) did not converge. To the west of the basin, where the thicker crust results in greater amplification of the short-wavelength anomalies when downward continued to the crust-mantle interface, this model predicts pervasive undulations of ~30 km in crustal thickness due to instabilities in the model that mask any possible signature of the rings. Even in the eastern half of the basin where the crust is thinner, large instabilities in the modeled crust-mantle interface develop within the ring system. Such large magnitude relief along the crust-mantle interface is not physically realistic, and this model is of limited usefulness in interpreting the structure of the basin. These large-amplitude undulations in the modeled crust-mantle interface are likely a result of the amplification of gravity anomalies arising from shallow density anomalies within the crust as discussed in Section 2.4. These instabilities could only be fully suppressed for a simple degree-dependent filter when the filter had an amplitude of 0.5 at degree 80, as previously found by Wieczorek et al. (2013).

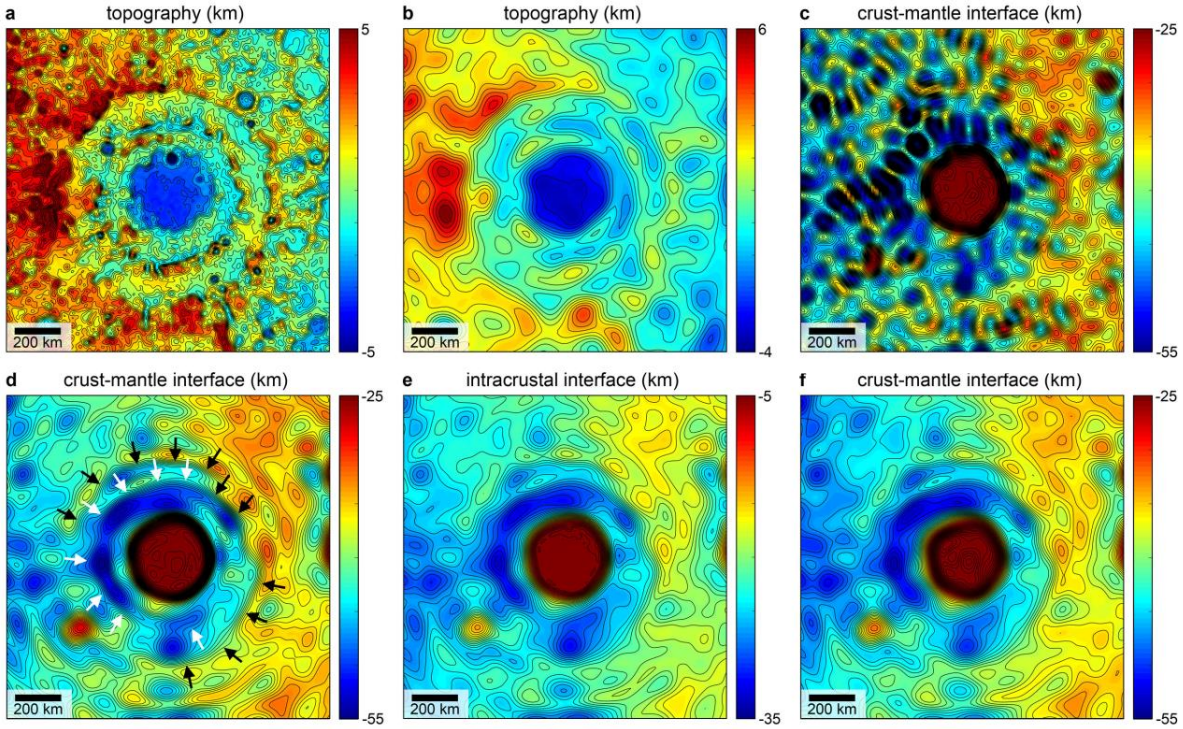

Figure 7. Topography and crustal thickness models of Orientale. **a** The topography of the basin was **b** filtered with the same degree- and order-dependent filter used during crustal thickness modeling for comparison with the crustal models. **c** A crustal thickness model with a simple degree dependent low-pass filter between degrees 130 and 150 (slightly lower radial resolution than the models in d-f) shows large amplitude undulations along the crust-mantle interface. Models of the relief along the crust-mantle interface and a possible intra-crustal interface for a uniform (**d**) and layered (**e-f**) crust show closely spaced contour lines at inflections interpreted to be offsets across the ring faults. Inflections interpreted as the subsurface manifestations of the Outer Rook and Cordillera ring faults are indicated by white and black arrows, respectively, in **d**. All maps are in a simple polar projection centered on the basin.

Using the degree- and order-dependent filter to achieve higher radial resolution and more smoothing in the azimuthal direction (see Appendix A.4), the modeled relief along the crust-mantle interface is much smoother in all parts of the basin. Contour plots of the relief along the crust-mantle interface for the single layer (uniform density) crust show distinct downward inflections at the approximate locations of the Outer Rook and Cordillera rings, consistent with offsets across these interfaces caused by the ring faults (Fig. 7d). The relief along both the intra-crustal and crust-mantle interfaces for the layered model shows similar undulations at the rings

with smaller magnitudes (Fig. 7e-f). In profile, the undulations at the rings in these models resemble the azimuthally averaged pre-GRAIL models of Andrews-Hanna (2013), but the new models have higher radial resolution and are now azimuthally-resolved. The similarly filtered topography highlights the ring structures at the surface without any obvious artifacts of the filtering process (Fig. 7b).

By resolving the subsurface structure of the rings in map view, these crustal thickness models reveal new information about the geometry of the ring faults in three dimensions. Average profiles through the crustal thickness models across azimuths showing similar structure were used to better constrain the fault geometry (Fig. 8). The subsurface manifestations of both the Outer Rook and Cordillera ring faults are most clearly expressed in the NW sector of the basin (Fig. 8a-b). The subsurface expression of the Cordillera fault is shifted toward the basin center relative to its surface expression, as expected for an inward dipping fault, leading to a calculated dip of 71° for the uniform crust or of 60° for the layered crust. The subsurface expression of the Outer Rook fault is aligned with its surface expression, leading to a calculated fault dip of 90°.

The amplitudes of the undulations interpreted as ring fault offsets across the subsurface density interfaces should match their surface expressions in the similarly filtered topography. The topographic step across the Cordillera fault in the NW quadrant of 1.1 km in the detrended filtered topography is similar to the step of 1.3 km across the detrended intracrustal and crust-mantle interfaces in the layered crust model, but much less than the step of 3.3 km in the uniform

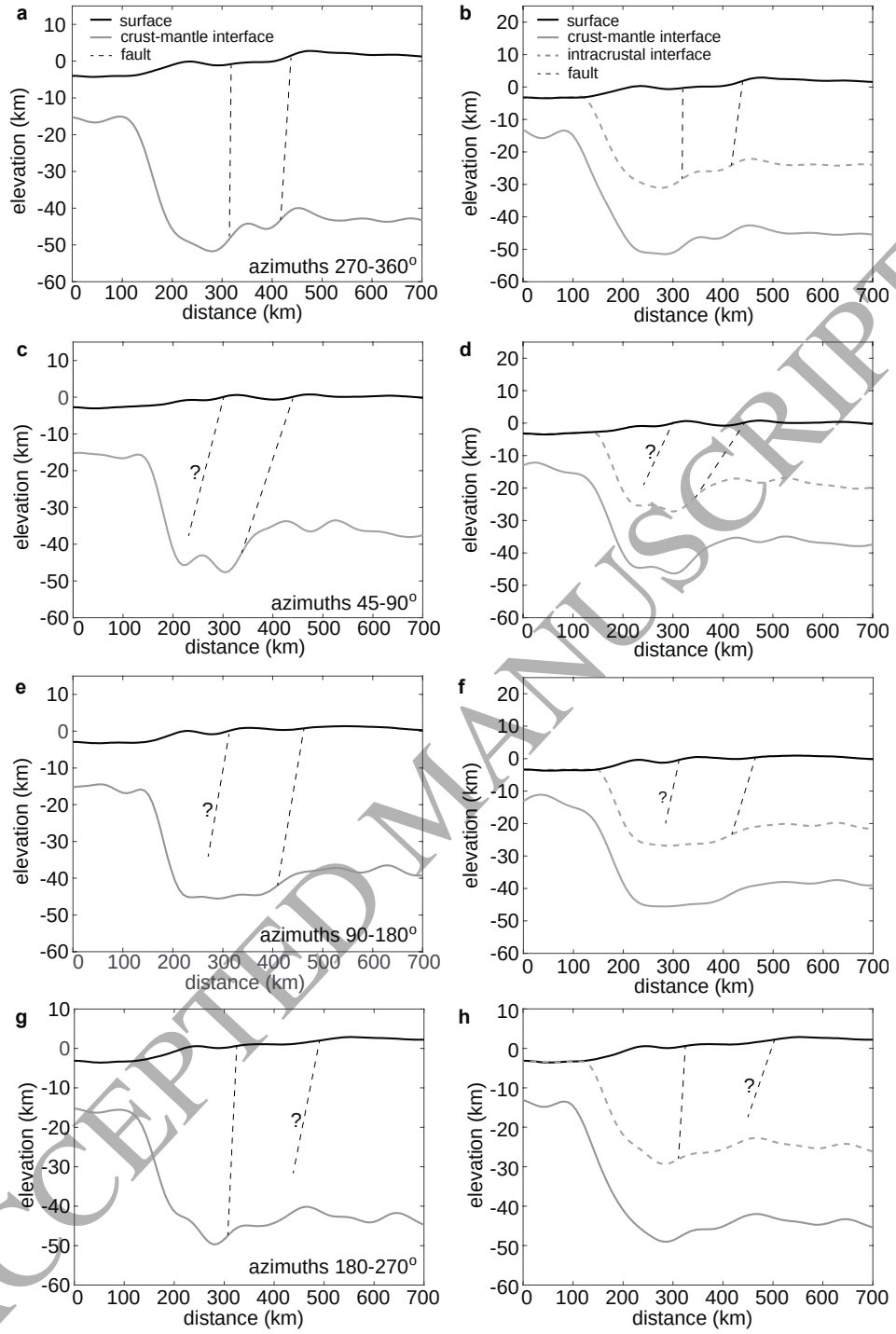

Figure 8. Average radial profiles through the single layer (left) and two layer (right) crustal thickness models, across azimuths 270°-360° (a,b) and 45°-90° (c,d), 90-180° (e-f) and 180-270° (g-h). Interpreted fault structures are traced between the inflection points at the interfaces. For the two layer models, faults are only drawn from the surface to the intracrustal interface, but are interpreted to extend to the crust-mantle interface as well (see text for discussion). Faults with uncertain interface crossings based on either the profiles or the map view are indicated with question marks. The basin center lies at a distance of 0 km.

crust model (Fig. 8a-b). Models in which all of the short wavelength gravity anomalies were ascribed to relief along the intra-crustal interface (not shown), representing faults that extend to mid-crustal depths but terminate in the lower crust, generated too much relief along this interface. This result favors a structure in which the density increases with depth in the crust, and faults extend down to and offset the crust-mantle interface. The similar amplitude in relief along the crust-mantle interface and the surface, combined with the fact that fault displacement typically tapers down-dip to zero at the lower fault tip (Cowie and Scholz, 1992), suggests that the faults extend to great depths within the mantle. Furthermore, this similarity in amplitude confirms that the crustal thickness model is physically realistic, and is not misattributing short wavelength gravity anomalies arising at shallow depths as instead being sourced from relief along the crust-mantle interface (as observed in Fig. 7c).

Progressing clockwise around the basin, the subsurface expression of the Cordillera fault is shifted toward the basin center in the NE quadrant between azimuths of 45° and 90° (Fig. 8 c-d; Fig. 7d, black arrows). The subsurface expression of the Cordillera appears to be continuous with that of the Outer Rook to the west, though that is likely due to the low resolution of the crustal thickness models. The lack of a Cordillera fault inflection further out and the location of this inflection further from the basin center than the topographic expression of the Outer Rook support the interpretation of this structure as the subsurface expression of the Cordillera rather than the Outer Rook. This geometry indicates a reduction of the Cordillera fault dip to angles of 22° or 13° for the uniform or layered crust models, respectively.

The lack of a distinct signature of the Outer Rook fault in the NE quadrant can be explained by a low-angle fault that intersects near the central mantle uplift and goes undetected,

consistent with the gravity gradient signature of a lower angle dike in this quadrant. An inflection in the averaged profiles could be interpreted as the signature of this ring fault leading to a dip of 36° or 21° (uniform or layered crust, respectively), overlapping with the range of uncertainty in the dip of the ring dike in this quadrant. However, this interpretation is not strongly supported by the contour maps.

The very low fault dips inferred in this quadrant motivate consideration of alternative interpretations. A steeply dipping Outer Rook fault, similar to that observed elsewhere around the basin, may intersect the crust-mantle interface at a similar radius as the low angle Cordillera fault, such that the two separate inflections cannot be resolved by the model. This interpretation is supported by the fact that the crust-mantle interface between the Outer Rook and Inner Rook in this quadrant is at a similar depth to that in the northwest quadrant where it has been offset downward by two separate ring faults. Alternatively, the Cordillera fault may terminate within the crust, such that only the expression of the Outer Rook fault is observed at the crust-mantle interface. However, this interpretation is difficult to reconcile with the layered crust model (requiring the fault to terminate above the intra-crustal density interface), and is at odds with the presence of maria ponds and a ring dike in this quadrant that are suggestive of magma using the fault as a conduit to pass through the crust. A low-angle Cordillera fault combined with an Outer Rook fault that terminates at shallow depths in the crust could also be consistent with the gravity, but the presence of the ring dike supports a deeply penetrating Outer Rook fault to act as a magma conduit through the crust.

The low Cordillera dip angle and possible low Outer Rook dip angle from the crustal thickness models in this quadrant are consistent with the low dip angles inferred from the shorter wavelength gravity gradient analysis of the ring dike and ring fault from the previous section.

Interestingly, this range of azimuths correlates with the up-range direction of the projectile that excavated the basin (Schultz and Papamarcos, 2010), suggesting that the collapse of the transient cavity and resulting ring faulting (Johnson et al., 2016; Potter, 2015) may have varied with azimuth relative to the projectile motion. However, these azimuths are also characterized by thinner crust, suggesting that the observed asymmetry in basin structure could instead, or in addition, be a result of the pre-existing asymmetry in crustal thickness.

In the southeastern quadrant, only the subsurface expression of the Cordillera ring is observed (Fig. 8e-f). This inflection is located further from the basin center over this range of azimuths than in the northeastern quadrant, resulting in a mean fault dip of 43° or 28° for the uniform or layered crust models, respectively. The subsurface location of the Outer Rook ring fault is not clear in the profiles, but the contour maps show that a steeply dipping Outer Rook ring fault (i.e., aligned with its surface expression) appears near an azimuth of 150°, similar to that observed in the southwestern quadrant.

In the southwestern quadrant (Fig. 8g-h), the expression of the Cordillera ring is complicated by the presence of the pre-existing Orientale Southwest impact basin (Neumann et al., 2015b). The model of the crust-mantle interface relief in this quadrant also becomes somewhat noisier due to the greater crustal thickness (and thus greater amplification of gravity anomalies of shallow origin when downward continued to the base of the crust). The subsurface expression of the Outer Rook reappears in this quadrant, with a dip of 73° or 75° for the uniform or layered crust models, respectively. Given the half-wavelength resolution of the crustal thickness model of 36 km, these dips are effectively identical and indistinguishable from 90°, in agreement with the gravity gradient signature of a vertical ring dike. Similarly, the uncertainty

in the ring dike dip from the gravity gradient inversion is consistent with the dip calculated from the crustal thickness model.

4. Summary and discussion

4.1. Summary of key results

The existence of rings around lunar basins has long been recognized (Hartmann and Kuiper, 1962), but only recently has new data made a quantitative understanding of the properties of those rings possible. These analyses of GRAIL gravity data reveal direct evidence for the shallow and deep crustal structure of basin rings around Orientale. The results of these analyses confirm the presence of ring faults and ring dikes, both of which were first postulated by Hartmann and Kuiper (1962) using Earth-based images.

The innermost major subsurface structure revealed by both the gravity gradients and the crustal thickness model is interpreted as the edge of the excavated cavity, within which the crust has been thinned by the impact. Hydrocode models indicate that the Inner Rook formed when the collapsing central uplift overran the thickened and overturned crust outside the excavated central cavity (Johnson et al., 2016), similar to the peak-ring of the Chicxulub basin on Earth (Morgan et al., 2016). The outer edge of this cavity in the subsurface at a radial distance of 180 km is ~50 km closer to the basin center than the edge of the Inner Rook Montes, consistent with an inward translation of deep material during the collapse of the basin. A more subtle gravity gradient anomaly at approximately the same radial location may be the expression of the edge of the solidified melt pond within the basin center associated with the inner depression.

The gravity gradient signature of the shallow structure of the Outer Rook is dominated by the effect of a ring dike intruded into the ring fault. While the extrusive maria deposits within

this ring are discontinuous and limited to the eastern parts of the basin, the ring dike fully encircles the basin without interruption. The volume of the dike within the crust of ~2.4×10^5 km^3 exceeds the inferred volume of the extrusive mare basalt within the basin (Whitten et al., 2011) by a factor of ~18, showing the important role of intrusive activity in the post-impact volcanic and magmatic evolution of the basin. The Outer Rook ring dike is nearly vertical around most of the basin, but has a dip of ~47° in the northeastern quadrant. Crustal thickness models reveal an inflection along the crust-mantle interface at the Outer Rook that is aligned with surface expression of the ring in the western half of the basin, indicating a steeply dipping to vertical fault. In the northeastern quadrant, the expression of the Outer Rook ring fault at the crust-mantle interface becomes indistinct and may merge with the uplifted mantle plug in the basin center, supporting a lower fault dip consistent with the gravity gradient signature of the dipping ring dike.

Over most of its extent, the Cordillera ring gravity gradients support the existence of a shallow density interface that has been offset by the ring fault, possibly representing the base of either the ejecta blanket or a deeper megaregolith layer. The crust-mantle interface shows a discrete inflection at the Cordillera, indicating a deep offset across this ring fault. The fault dips from the crustal thickness models range from 60-71° in the northwestern quadrant, to 13-22° in the northeastern quadrant. However, there is some ambiguity in the interpretations of the northeastern quadrant, since only one of the Outer Rook and Cordillera is clearly expressed in the modeled crust-mantle interface there. The predicted relief along the subsurface interfaces at the Cordillera and Outer Rook ring faults approximately match the surface relief when an intra-crustal density interface is included in the models, supporting an increase in the density of the crust with depth (Besserer et al., 2014).

The shallow and deep structure of the faults indicated by the gravity gradients and crustal structure models are broadly consistent. Both analyses indicate near vertical faults for much of the Outer Rook, and lower angle faults for the Cordillera. Both analyses also support lower fault dips in the northeastern quadrant for both the Outer Rook and Cordillera, possibly due to the fact that this is the up-range direction of the basin-forming projectile motion (Schultz and Papamarcos, 2010), or due to the thinner pre-impact crust in this quadrant. Future hydrocode models of basin collapse and ring formation (Johnson et al., 2016) may be able to distinguish between these two hypotheses. The consistency of the fault dips in the shallow crust revealed by the gravity gradients and the deep crust revealed by the crustal thickness models indicates that the fault dips remain largely constant within the crust, rather than transitioning to listric faults at depth within the crust. The large fault offsets at the crust-mantle interface indicate that the faults likely extend to much greater depths in the mantle, consistent with predictions of hydrocode models (Johnson et al., 2016).

4.2. Comparison to previous studies

These results are broadly consistent with previous analyses of the fault dips. Kattoum and Andrews-Hanna (2013) used a different approach with pre-GRAIL gravity data to constrain the Cordillera fault dips to be in the range of 20-60°, consistent with the range of dips found in this study. However, that study was unable to confirm the presence of an Outer Rook fault or to constrain the variation in fault properties with azimuth around the basin. More recently, Zuber et al. (2016) generated azimuthal averages of higher resolution global crustal thickness models and found results consistent with 50° fault dips along both the Cordillera and Outer Rook faults to the north and south of the basin. For the Cordillera, the fault dips from that study are gentler than

those of this study for the NW quadrant and steeper than those of this study for the NE quadrant, suggesting that that study may have captured the transition in dip across these azimuths. Although the interpretation of a 50° Outer Rook fault dip in Zuber et al. (2016) is at odds with the vertical fault in some parts of the basin supported by this analysis of the gravity gradients and crustal structure, the profiles of the crust-mantle interface in that study also show an inflection immediately beneath the Outer Rook south of the basin that could be interpreted as the signature of a vertical fault. Nevertheless, we note that the dips from Zuber et al. (2016) are more consistent with the model predictions of Johnson et al. (2016).

Nahm et al. (2013) used mechanical models of faulting in comparison with the observed topography to constrain the Cordillera fault dips to be in the range of 61-75°, and the Outer Rook fault dips to be in the range of 70-80°. Although our results suggest steeper dips for the Outer Rook and gentler dips for the Cordillera than that study, both studies agree that the Outer Rook fault dips more steeply than the Cordillera fault. However, Nahm et al. (2013) found depths of faulting of 19-37 km, suggesting that the faults terminate within the crust, whereas our work finds that the gravity data requires faults extending down to and offsetting the crust-mantle interface. This difference is significant since the depth of faulting has important implications for models of ring formation, as discussed below. In reconciling this discrepancy, we note that mechanical models of faulting depend on a number of parameter assumptions that may yield non-unique results, and also rely on the assumption of elastic deformation in a semi-infinite half-space. Furthermore, the formation of ring faults in the highly dynamic process of basin collapse (Johnson et al., 2016) may violate the assumption of mechanical models that all deformation outside of the faults is purely elastic.

4.3. Comparison to Chicxulub

The Chicxulub basin on Earth, for which detailed structural information is available from analyses of seismic, gravity, and magnetic data (Gulick et al., 2013), provides an interesting point of comparison (see also Nahm et al., 2013). However, while simple gravity scaling of the diameters of the innermost peak rings suggest they should have comparable structures ($D_{Chicx} \times g_{Earth}/g_{Moon}$ = 80 km×9.8/1.6=490 km; $D_{Orientale,IR}$ = 464 km), important differences exist that caution against a simple comparison. In particular, the central depression of Orientale exhibits an uplift of the crust-mantle interface by 25-30 km, whereas seismic and gravity data from Chicxulub reveal that structural uplift of ~10 km within the peak ring is largely confined to the crust, with only ~2 km of uplift of the crust-mantle interface (Christeson et al., 2009; Vermeesch and Morgan, 2008). This difference between the two basins can likely be ascribed to the difference between the excavation depth relative to the crustal thickness, with Chicxulub excavating only the upper ~1/3 of the crust, and Orientale excavating the majority of the crustal column. Similarly, evidence from lunar basins over a wide range of sizes shows that interaction of the transient cavity with the mantle exerts an important control over the final mantle uplift (Baker et al., 2017), with the depth of melting also likely playing a role (Baker et al., 2015, 2011). Notably, both the diameter of the central region of structural uplift of ~80 km and the central positive Bouguer anomaly of ~15-20 mGal of Chicxulub (Vermeesch and Morgan, 2008) place it at the lower end of diameters and magnitudes of observed positive Bouguer anomalies indicative of structural uplift in lunar basins (90 km and 40 mGal, respectively; Neumann et al., 2015b).

While Orientale exhibits two distinct major outer ring faults (the Outer Rook and Cordillera) with displacements of 1-5 km (Nahm et al., 2013), interpreted seismic sections show

that the central depression and peak ring of Chicxulub are surrounded by ~15 evenly spaced faults with most displacements in the range of meters to tens of meters that are loosely grouped into a terrace zone, inner ring, and outer ring (Gulick et al., 2013, 2008). Only the innermost inner ring fault of Chicxulub (referred to as the inner rim), with a throw of 300-950 m (Gulick et al., 2008), approaches the scale of the Orientale ring faults. The ratio between the radii of the inner rim (70-85 km) and peak ring (39-40 km) of Chicxulub of ~2:1 matches the ratio between the radii of the Cordillera (462 km) and Inner Rook (232 km), leaving the Outer Rook without direct analog in Chicxulub. In place of the Outer Rook (r=310 km), Chicxulub possesses a complex terrace zone consisting of 4-9 faults distributed uniformly between the peak ring and inner rim. The cumulative throw across faults in the terrace zone of 2-6 km exceeds that across the inner rim fault and is comparable to that across the Outer Rook fault of Orientale. Unlike the Outer Rook fault, these terrace zone faults do not appear to cross either the crust-mantle interface or the paleo-surface, having been buried beneath the proximal ejecta of the basin. Faults in the terrace zone and inner ring of Chicxulub have dips ranging from 45-70°, with most falling in the range of 50-60°. A multitude of small-displacement normal faults surround Chicxulub exterior to the inner rim. Similar minor faults exterior to the Cordillera on the Moon would not be detected in either topography data (due to the subsequent impact gardening of the surface) or gravity data (due to superposed small-scale density anomalies), but may nevertheless exist.

In terms of the gross structure of the main basin rings, Chicxulub more closely resembles a peak ring basin such as Schrödinger (Baker et al., 2017; Kring et al., 2016) or Schwarzschild, rather than a multiring basin such as Orientale (Gulick et al., 2013), despite gravity scaling of basin diameters that would indicate otherwise. This discrepancy is consistent with expectations that the impact excavation depth relative to the lithosphere thickness should control the

formation of outer rings (Johnson et al., 2016; Melosh and Mckinnon, 1978; Potter, 2015). However, unlike both Schrödinger and Orientale in which one or two major ring structures with large offsets surround the central peak ring and inner depression, faulting exterior to the peak ring of Chicxulub is more distributed with modest offsets across a large number of approximately equally spaced faults with only somewhat greater displacement across an inner rim fault.

Notwithstanding these differences, Chicxulub does demonstrate the importance of target variability in producing asymmetries in the final basin structure (Gulick et al., 2013, 2008). The Chicxulub impact overlapped with a pre-existing basin characterized by thinner crust. Seismic profiles overlapping with this pre-existing basin show the outer faults extending out to a radius of 97-114 km and continuing down to the crust-mantle interface, while seismic profiles in regions of thicker crust show faults extending out to a radius of 119-135 km and transitioning to a near-horizontal décollement at a depth of ~12 km (Gulick et al., 2013, 2008). In contrast, the major ring faults of Orientale all extend to the crust-mantle interface and show systematically lower dips in regions of thin crust. Although the ring radii of Orientale are somewhat asymmetric, the centroids of the Cordillera and Inner Rook are separated by only ~20 km in the north-south direction, and thus do not indicate control by either the asymmetry in crustal thickness or the projectile direction of motion.

It is also worth noting that only the major inner rim fault of Chicxulub appears to have played an important role in capturing groundwater flow, leading to a ring of cenotes at the surface (Gulick et al., 2013). This interaction of a ring fault with fluids may be loosely analogous to the capture of a dike by the Outer Rook ring.

4.4. Tectonic implications

Our results indicate a wide range of Cordillera fault dips (13-78°) varying with azimuth around the basin, and a vertical Outer Rook fault around much of the basin. These dips include values incompatible with simple Andersonian faulting (Anderson, 1905). However, Anderson's theory of faulting assumes hydrostatic vertical stresses and is best applied to faults that form through slip along pre-existing fractures in a large number of small individual events as a result of the slow accumulation of strain over geologically long periods of time. In contrast, the Orientale ring faults are likely to have formed from slip of several kilometers (Nahm et al., 2013) over a period of minutes during the dynamic collapse of the transient cavity (Johnson et al., 2016). Hydrocode models show ring faults forming while the ejecta is still falling and the surface is continuing to undergo vertical motions in excess of 10 km (Johnson et al., 2016). Under such conditions, Anderson's theory of faulting may be of limited applicability. It is tempting to explain the low fault dips of the NE quadrant by analogy to the low angle Heart Mountain detachment, which also involved rapid slip on a low angle fault (Beutner and Gerbi, 2005), though important differences exist in both the setting and tectonic geometry, and this leaves the steep to vertical faults elsewhere around Orientale unexplained. Any explanation for the fault dips must account for the asymmetries around the basin as well as the systematically steeper dips for the Outer Rook than the Cordillera. Low dips to the NE may be a result of this being either the uprange direction of the projectile or a region of thinner crust, but there is no compelling reason to expect either of these effects *a priori*.

4.5. Comparison to other basins

These results also have important implications for other basins. Future work will examine the structure of a wider set of lunar basins using gravity gradiometry and crustal thickness models (see also Andrews-Hanna et al., 2013b). A qualitative global survey reveals the gravity gradient signatures of ring dikes to be common around lunar basins (Fig. 2), including some that are not associated with volcanic maria on the surface (e.g., Korolev). Some basin rings that are very poorly expressed in topography are seen clearly in the gravity gradients because of the presence of ring dikes (e.g., the middle ring of Nectaris, the outer ring of the proposed Fowler-Charlier basin (Neumann et al., 2015b)). The magnitudes of the ring dike anomalies appear to be greater for basins formed in thin crust (e.g., Nectaris, Smythii, and Apollo) than for basins formed in thick crust (e.g., Korolev), supporting the idea that thicker crust inhibited the rise of magma due to buoyancy effects (Head and Wilson, 2017). A number of farside basins lack ring dike signatures, including Hertzsprung, Freundlich-Sharonov, and Mendel-Rydberg. Nevertheless, basins with and without ring-dike signatures are found on both hemispheres.

The negative gravity gradients interpreted as ring dikes are the dominant signatures seen in the global filtered gravity gradient map (Fig. 2), suggesting that ring dike intrusions featured prominently in the magmatic evolution of the entire Moon. Although the specific timing of ring dike formation is unknown, both the ring dikes and major maria formed after the basins and may have been contemporaneous. A link between the ring dikes and the maria is further supported by the association of the Outer Rook and partial Cordillera ring dikes with small mare ponds. It thus seems probable that these ring dikes record the intrusive phase of magmatic activity that was the counterpart to the extrusive eruptions that formed the maria. The maria deposits within basin cavities would have extruded through the complexly fractured sub-cavity crust, while the ring dikes took advantage of the pre-exising ring faults. The ring dikes are similar in width to

the randomly oriented linear intrusive bodies that pre-date the ancient cratered surface and thus formed very early in lunar history (Andrews-Hanna et al., 2013a). However, the ring dikes must post-date the associated impact basins, and thus largely formed later than ~3.8 billion years ago. The transition from the formation of randomly oriented linear intrusions to the formation of ring dikes suggests a change from an early period of isotropic stress in the lunar crust (Andrews-Hanna et al., 2013a), to a later period in which stresses and magma ascent were locally controlled by the presence of basins and their associated mascons (McGovern et al., 2014; Solomon and Head, 1980, 1979).

The paired positive and negative gravity gradient anomalies found at the Cordillera ring are not found in association with rings around most other basins. Similarly, most basins also lack evidence for the low density ejecta blanket inferred to be present around Orientale (Wieczorek et al., 2013) which we invoke to explain the observed gravity gradient signature. Seismic shaking from subsequent impacts appears to have a substantial effect on both the roughness (Kreslavsky and Head, 2012) and density (Wieczorek et al., 2013) of these older basin ejecta deposits.

4.6. Implications for basin ring formation

The subsurface structure of Orientale places important constraints on the mechanism of ring formation. Although other hypotheses have been proposed (Baldwin, 1972; Hodges and Wilhelms, 1978; Zeng-Yuan et al., 1990), the main theories for explaining basin ring formation are the megaterrace/nested melt cavity model (Head, 2010, 1974) and the ring tectonics model (Melosh and Mckinnon, 1978). For the formation of the outermost rings, these models are broadly similar in that they both invoke the collapse of the transient cavity to drive exterior ring

faulting. The primary difference between these two models is the distribution of deformation with depth. The megaterrace model invokes a low-angle listric fault that is confined within the crust until it intersects the surface within the central cavity of excavated crust, causing inward slumping similar to the terraces in complex craters (Head, 2010, 1974). In contrast, the ring tectonics model invokes a steeper fault that extends down into the mantle, where it connects with deeper material undergoing ductile deformation as mantle material flows toward and up into the central basin as the basin floor rebounds (Melosh and Mckinnon, 1978). Observations from topography, gravity gradients and crustal thickness models demonstrate that the ring faults at both the Outer Rook and Cordillera extend from the surface to the crust-mantle interface, requiring a deep-seated mechanism to drive ring formation. The fact that these faults later acted as conduits for magmatic intrusions further supports their penetration to great depths. The similar fault dips inferred at shallow and deep crustal depths in this study do not support listric behavior of the faults within the crust. The inward translation of the edge of the excavated crustal cavity in the subsurface relative to its surface expression is supportive of an inward flow of deep material toward the basin center after the impact.

Recent hydrocode modeling has predicted the formation of localized shearing along fault-like structures through a process resembling the ring tectonics model (Johnson et al., 2016; Potter, 2015; Potter et al., 2013). Those models predict faults extending well into the mantle, consistent with the structure revealed by GRAIL. However, the similar dips of the Outer Rook and Cordillera faults in the hydrocode models of 50-55° (Johnson et al., 2016) are at odds with the range of dips, the differences between the Outer Rook and Cordillera, and the prominent asymmetries around the basin observed in this study. This discrepancy may be explained by effects not included in those hydrocode models, such as an oblique impact or the inclusion of a

strain-rate dependent rheology (see discussion in Johnson et al., 2016). Thus, although great strides have been made in understanding basin ring faults from both observational (Zuber et al., 2016) and modeling (Johnson et al., 2016; Potter, 2015; Potter et al., 2013) perspectives, continued work is needed to more fully understand the details of ring formation around Orientale as well as other basins. Nevertheless, these recent advances in both numerical modeling and gravity analyses are converging on an understanding of the outer basin rings as inward dipping normal faults cutting through the entire crust driven by the inward flow of deep mantle material during the collapse of the transient cavity.

Acknowledgements. This work was supported by grant NNX16AT32G from the NASA GRAIL Guest Scientist Program and grant NNX17AK53G from the NASA Lunar Data Analysis program to JCAH. BCJ was supported by grant 80NSSC17K0341 from the NASA Lunar Data Analysis Program. We are grateful to Amanda Nahm and an anonymous reviewer for their helpful and insightful comments.

Appendix. Methods

A.1. Gravity gradients

All analyses used the JGGRX_1500E gravity model with a half-wavelength resolution of 3.6 km (Konopliv et al., 2014; degree 1500 model is available on the PDS). For the gravity gradients, the Bouguer gravity was first calculated using a topographic correction that accounts for the effects of the finite amplitude of topography, and using the spatially variable crustal density determined from the GRAIL data (Wieczorek et al., 2013). Tests using a uniform density of 2550 kg/m^3 yielded similar results, showing that the results are not sensitive to this choice. For the gravity gradient calculation, a high-pass cosine-shaped taper was applied between degrees 40 and 60 in order to minimize the large anomalies associated with the mantle uplift beneath the center of the Orientale basin and better highlight the small-scale structures associated with the rings. A low-pass taper was applied between degrees 350 and 650 to minimize the striping parallel to the orbit tracks of the spacecraft that occurs at wavelengths comparable the spacing between adjacent orbits in higher degree expansions. The width of the low-pass taper was chosen based on the competing desires to minimize ringing around discrete features (based on filtered forward models of gravity gradients associated with dikes), and to minimize the filter width so as to retain as much signal as possible without extending into degrees that show orbit striping. The Monte Carlo inversions of the gravity gradients applied a similar filter to the forward models as discussed below. The chosen low-pass filter yields a gravity gradient map that shows no orbit-parallel striping within Orientale, and is globally well behaved with modest striping only in the South Pole-Aitken and Imbrium basins.

Gravity gradients were calculated using the eigenvalues of the second horizontal derivatives of the Bouguer potential, and are given in units of Eötvös (E), where 1 E is 10^{-9} s^{-2}.

The eigenvalues of the gravity gradient tensor were calculated, and the eigenvalue of maximum amplitude (be it positive or negative) at each point on the surface was adopted as the value at each point. This approach has the effect of calculating the gravity gradients orthogonal to the dominant structure at each point on the surface, and is useful for highlighting small-scale structures such as dikes and faults in the shallow subsurface (Andrews-Hanna et al., 2013a).

At these high degrees, the effect of the variable elevation of the lunar surface becomes prominent. The magnitudes of the gravity gradients attenuate with distance d from the sources of the anomalies as $1/d^3$, rather than $1/d^2$ for the gravity anomaly or $1/d$ for the potential. As a result, when the gravity gradients are calculated on a spherical surface at the mean planetary radius, they have much lower magnitudes over the nearside where the elevation of the physical surface is below the mean planetary radius, and much greater magnitudes over the farside where the elevation of the physical surface is above the mean planetary radius (Fig. A1). This effect is pronounced around Orientale, which is situated on an east-west slope between the nearside and the farside. To avoid these artificial variations in the magnitudes of the gradients, we calculated the gravity gradients on a smooth (spherical harmonic degree 50) representation of the surface topography. This surface follows the physical surface over long wavelengths but is smooth on the scale of the gravity anomalies of interest (degrees greater than 50, based on our chosen high-pass filter for the gravity data). The chosen low-pass filter cutoff at degree 50 for the surface model is at a much longer wavelength than the gravity anomalies and gravity gradients associated with the shallow structure of the Outer Rook and Cordillera rings (with a typical half-wavelength of ~35 km, equivalent to spherical harmonic degree 156). This approach was implemented by calculating the eigenvalues of the gravity gradients on spherical surfaces at reference radii in 200 m increments, and interpolating to find the value at each point on the

smoothed surface. Calculation of the gravity gradients on this smooth surface results in similar amplitude anomalies across both the near and far sides (Fig. 2). This approach allows direct comparison of the gravity gradients at any point on the surface regardless of elevation (e.g., for comparison of different azimuths around the Orientale basin despite the very different elevations, or for comparisons of basins in different areas of the Moon), while simultaneously providing a reference surface that is locally smooth to enable analysis of small-scale gravity anomalies. Manipulations of the gravity data were performed with the SHTOOLS software package (Wieczorek, 2014).

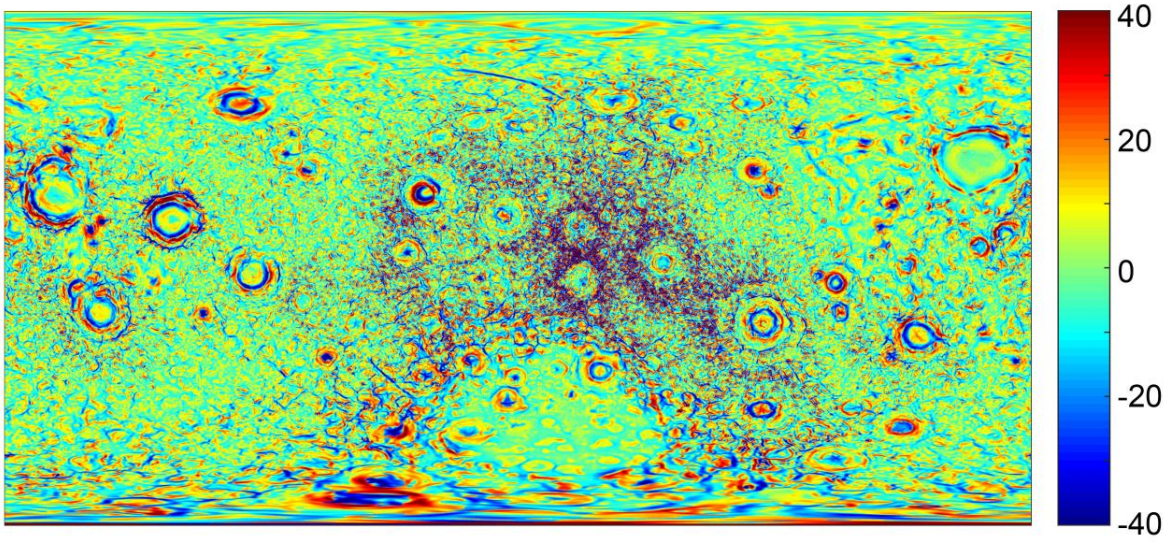

Figure A1. Global gravity gradient map (in Eötvös) as calculated on spherical surface at the mean planetary radius. Map is in a cylindrical projection centered on the lunar farside.

A.2. Gravity gradient profile alignment

Prior to averaging the gravity gradient profiles across a feature of interest, we stretched and aligned the profiles as described below. This alignment was necessary because the rings are not perfectly circular in their expressions in either gravity or topography data. An average of the

original non-aligned ring profiles would result in broader and smoother anomalies of lower amplitude. We first calculated profiles through the gravity gradients along great circle paths radiating out from the center of the basin (chosen to be 20.1°S 265.2°E as the approximate center of the ring system in the gravity gradients). In order to account for the fact that none of the rings are exactly circular, we then used an iterative approach to stretch the individual profiles so as to align the rings across different profiles. We first isolated short sections of the radial profiles around each ring of interest (Inner Rook, Outer Rook, or Cordillera). The average of the profiles within ±10° of azimuth of a given direction was compared with the full average of all profiles around the basin. The locally averaged profiles were aligned with the basin average by implementing successive radial shifts toward or away from the basin center, and calculating the cross-correlation relative to the average profile for each shift. The optimal shift for each profile segment of each ring was determined to be the one with the greatest cross-correlation to the average profile. For each radial profile, a linear stretching function was then applied to each segment between one ring and the next in order to align the rings with the average profile. The above approach was then iterated 15 times, using the average profiles from the previous shifts to compare with the raw profiles in order to determine the optimal shifts in the next iteration.

The above approach allows for an objective alignment and averaging of the basin rings free from user input and bias (Fig. A2), while reducing the sensitivity to the asymmetries of the rings and the chosen basin center. Although it would be possible to manually line up the maxima/minima in the gravity gradients more exactly at a particular ring prior to averaging in order to produce a stronger anomaly in the averaged profile, this has potential to introduce user bias by artificially aligning the random background anomalies and could even generate dike- or fault-like features in the average profiles where none exist in reality. Given the similar

amplitudes of the background variability and the gravity gradients associated with the rings, the above objective and automated approach is preferred. Nevertheless, the average profile after alignment may under-represent the magnitude of the maxima and minima at the rings due to some persistent misalignment, and thus the dike volume for the Outer Rook and density contrast across the fault for the Cordillera may be underestimates. The average of the non-aligned profiles is similar to the average of the aligned profiles, but exhibits lower amplitudes at the rings and more variability around the rings.

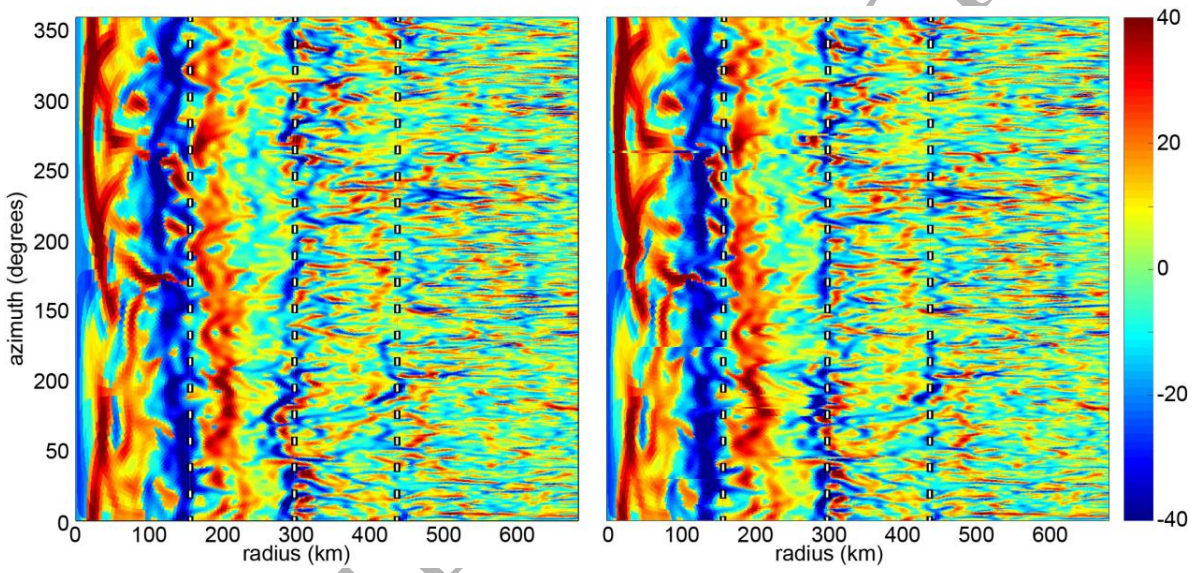

Figure A2. Gravity gradients as a function of radius from the basin center and azimuth measured clockwise from north before (**a**) and after (**b**) alignment of the individual profiles. The approximate locations of the Inner Rook, Outer Rook, and Cordillera rings are shown by the vertical dashed lines (centered on the paired positive and negative gradients of the Inner Rook and Cordillera, and the negative gradients of the Outer Rook).

A.3. Gravity gradient inversions

The gravity gradient profiles were inverted using a Metropolis-Hastings Markov-chain Monte Carlo model in order to identify the optimal model parameters and their associated uncertainties (Andrews-Hanna et al., 2013a; Metropolis et al., 1953). This model generated

forward models of the gravity gradients arising from simple geometric structures. The gravity gradient in the *x* direction of a rectangular prism was calculated as:

$$U_{xx} = G\rho \sum_{i=1}^{2} \sum_{j=1}^{2} \sum_{k=1}^{2} arctan \frac{y_j z_k}{x_i r_{ijk}} \quad (1)$$

$$r_{ijk} = \sqrt{x_i^2 + y_j^2 + z_k^2}$$

where x_i, y_j, z_k represent the *x*, *y*, and *z*, components of the vector between the observation point and the centers of the different faces of the prism (Forsberg, 1984; Li and Chouteau, 1998). The gravity gradients of discrete structures are highly sensitive to the resolution at which they are measured or calculated, so the computed gravity gradients from the forward model were filtered in the Fourier domain to match the filter applied to the gravity gradients.

Dikes and faults were represented as rectangular prisms with the *z*-axis in the vertical direction, the *x*-axis in the direction radial to the basin, and the *y*-axis in the horizontal direction along the strike of the structure. The structures were made to be sufficiently long (1000 km) in the along-strike direction, such that the ends of the structures have no impact on the predicted gravity gradients at their midpoints. Dikes with non-vertical dips were modeled by adjusting the angle of the reference surface on which the gravity was calculated and using the full gravity gradient tensor to calculate the gradient parallel to that surface. The forward model does not account for the curvature of the structures in map view around the basin. However, gravity gradients attenuate rapidly with distance as discussed above, so this curvature would have little effect on the results.

A.4. Crustal thickness modeling

We first rotated the center of Orientale (here taken to be 19°S, 265.5°E to more closely align with the center of the positive Bouguer anomaly) to the pole, in order to align the symmetry

axis of the basin with that of the spherical harmonic basis functions. We note that both the gravity gradient profile alignment and the crustal thickness modeling have been designed to naturally accommodate the asymmetries and irregularities in the rings, such that the results are not sensitive to the exact choice of basin center. Each spherical harmonic basis function of a given degree and order has differing resolutions in the radial and azimuthal directions, with the minimum azimuthal resolution occurring nearest the pole (Fig. A3a). For each spherical harmonic basis function, we calculated the minimum azimuthal resolution as:

$$\lambda_{min} = \frac{2\pi \cdot \sin(\phi)}{m} \tag{2}$$

where φ is the co-latitude of the maxima/minima of the basis function closest to the pole, and *m* is the order. We then constructed a filter *f* dependent upon both degree and order, so as to apply a cosine-shaped high-pass taper based on the desired minimum azimuthal resolution.

$$f(\lambda_{min}) = 0.5 \cdot \left(1 + \cos\left(\pi \cdot (\lambda_2 - \lambda_{min})/(\lambda_2 - \lambda_1)\right)\right) \Big| \begin{matrix} 1 \\ \\ 0 \end{matrix} \Big| \begin{matrix} \lambda_{min} > \lambda_2 \\ \lambda_1 < \lambda_{min} < \lambda_2 \\ \lambda_{min} < \lambda_1 \end{matrix} \tag{3}$$

where λ_1 and λ_2 bracket the desired minimum azimuthal resolution and λ_{min} is the minimum azimuthal resolution of a spherical harmonic basis function of a given degree and order. This filter was then multiplied by a more conventional degree-dependent filter in order to taper the radial resolution of the model. Because the minimum azimuthal resolution for each basis function occurs nearest the pole (at Orientale in the rotated reference frame), some smoothing occurs at longer wavelengths at lower latitudes as well. A similar but simpler approach was

taken by Andrews-Hanna (2013) using pre-GRAIL data, but that study used only the order zero spherical harmonic basis functions, thereby generating an azimuthally averaged crustal thickness model for Orientale extending out to degree 102 (corresponding to a half-wavelength resolution of 54 km).

Caution must be used in designing the filters, since large magnitude discrete anomalies can be artificially extended in the azimuthal direction to make ring-like structures, and coincidental alignments of smaller magnitude anomalies can be joined into a continuous ring. There is no single criterion for the optimal filter, since this depends on the magnitude and positioning of anomalies in a particular region. We investigated a wide range of filters, rejecting those that produced clearly artificial rings from isolated anomalies. The optimal model filter (Fig. A3c) combined a filter in the azimuthal direction with a cosine-shaped taper applied between azimuthal wavelengths of 4-6 degrees of arc (azimuthal resolution of 121-182 km), with a degree-dependent filter between spherical harmonic degrees 140-160 (radial resolution of 34-39 km). This filter largely avoids generating ring-like artifacts outside the basin. This model provides nearly a factor of 2 better resolution than the globally stable uniform resolution models of Wieczorek et al. (2013), and easily resolves the structures of the Outer Rook and Cordillera rings with their typical spacing of 100-120 km. More conservative models with lower radial resolution and/or less azimuthal smoothing generated similar structures. For comparison, a model applying only a simple degree-dependent cosine taper between degrees 60 and 80 does not resolve the rings as discrete inflections along the crust-mantle interface, while a model filtered between degrees 80 and 100 begins to resolve the Cordillera ring in the eastern half of the basin but cannot resolve the separate Cordillera and Outer Rook rings in the northwestern quadrant and exhibits unphysical oscillations outside the basin to the west (Fig. A4a). This latter model, while

lower in resolution than our primary model, confirms the location of the ring faults in the eastern half of the basin.

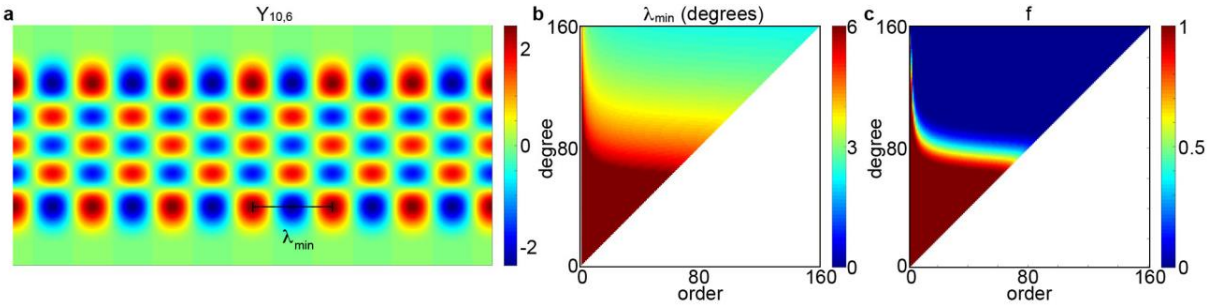

Figure A3. Spherical harmonic filter used in the crustal thickness modeling. **a** Global cylindrical projection map of an example spherical harmonic basis function at degree 10 and order 6 has a characteristic minimum azimuthal resolution (λ_{min}; measured in degrees of arc) that occurs in the row of maxima and minima closest to the poles. **b** The minimum azimuthal resolution was determined for each degree and order, and used to generate a filter **c** with a cosine-shaped taper between λ_{min} of 4 and 6 degrees of arc and between degrees 140 and 160 for use in the crustal thickness modeling.

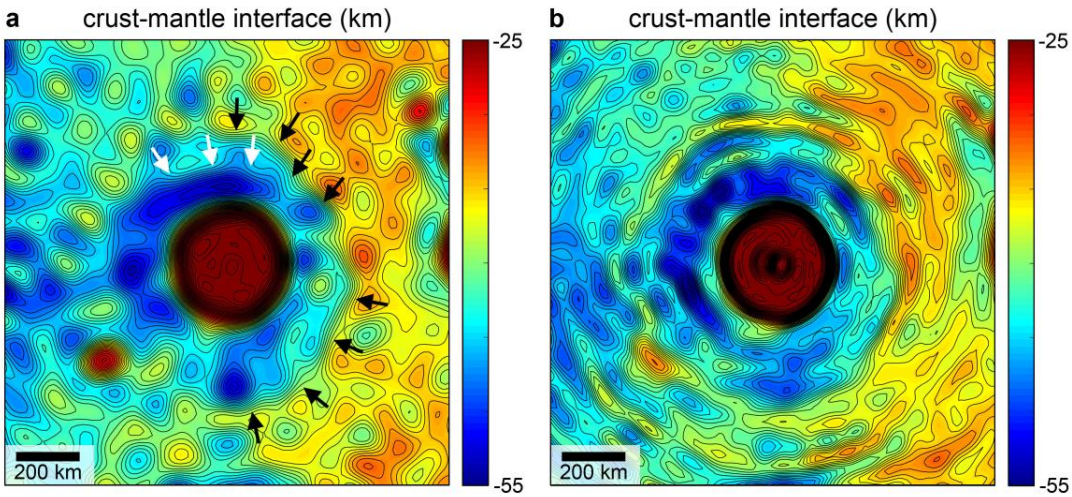

Figure A4. **a** Modeled crust-mantle interface for a simple degree-dependent filter with a cosine-shaped taper between 80 and 100 begins to resolve the basin rings in some locations (arrows) but is becoming unstable on the western side of the basin. **b** A model in which azimuthal smoothing was done in the spatial domain yields similar results to the spherical harmonic filtering approach.

Because there are shallow structures that are correlated with the basin rings, the azimuthal smoothing employed here does not remove all of the shallow signal from the gravity field. Even full azimuthal averaging may leave short wavelength gravity anomalies arising at shallow depths within the rings (e.g., dikes intruded into the ring faults, or offsets across shallow density interfaces). These anomalies, if downward continued to the crust-mantle interface and used to model crustal thickness, will result in erroneous large amplitude relief along the crust-mantle interface. We found the characteristic half-wavelength of the gravity anomalies and gravity gradients associated with the shallow structure of the Outer Rook and Cordillera rings to be ~35 km, corresponding to spherical harmonic degree 156. As a result, our models must be filtered such that these wavelengths are largely excluded. Our preferred Orientale model employs a filter with an amplitude of 0.1 at degree 156, thus excluding the majority of the signal arising from the shallow structure of the rings.

The crustal structure of Orientale was then modeled using the approach developed by Wieczorek and Phillips (1999). The gravity data was first corrected for the effects of topography to generate the Bouguer gravity. The Bouguer gravity was downward continued from the mean planetary radius to the mean radius of the crust mantle interface, assumed to be 34 km (Wieczorek et al., 2013). An iterative approach was then used to solve for the best-fit model of the spherical harmonic coefficients of the relief along the crust-mantle interface based on that Bouguer gravity. During the crustal thickness modeling, the degree and order-dependent filter described above was applied to the relief along the crust-mantle interface during each step of the iterative solution. Applying the filter instead to the Bouguer gravity directly would result in a similar solution, differing only because of the non-linear effects of the finite amplitude of the relief along the interface on the resulting gravity anomalies. A greater mean crustal thickness

(e.g., 43 km; Wieczorek et al., 2013) would increase the amplification of short wavelengths during downward continuation, resulting in somewhat greater amplitudes of the undulations along the crust-mantle interface at the basin rings, but would not otherwise change the nature of the results.

The two-layer crust models force the intra-crustal interface to lie parallel to the crust-mantle interface, except where this condition would cause it to rise above the surface, at which point the intra-crustal interface was set equal to the surface. These assumptions were implemented using spherical harmonic filters designed such that the fractions of the downward continued gravity anomalies attributed to the crust-mantle and intra-crustal interfaces are proportional to the assumed density contrasts across those interfaces, and an iterative scheme was used to prevent the intra-crustal interface from rising above the surface. A similar approach was used for axisymmetric models of the crustal structure of Orientale using pre-GRAIL data (Andrews-Hanna, 2013). The resulting models are consistent with the expected structure around an impact basin, with the majority of the crustal thickening in the ejecta outside the basin occurring in the upper crust, and with an intra-crustal interface that parallels the crust-mantle interface where both have been offset by the basin ring faults. Although an infinite number of alternative assumptions and models are possible, any model with an increase in density at an intermediate depth within the crust will yield qualitatively similar results.

We also tested models in which the azimuthal smoothing was done in the spatial domain rather than the spherical harmonic domain (Fig. A4b). This approach used a moving smoothing kernel that took on a value of 1 within ±2° of arc on the surface, and followed a cosine-shaped taper to 0 between ±2° and ±3° of arc, for a full kernel width of 6° of arc. This smoothing kernel was then used to generate a moving azimuthal average. The filtering in the radial direction again

used a simple degree-dependent spherical harmonic filter, this time between degrees 120 and 140 for model stability. The spatial domain approach has the advantage of imposing the differing radial and azimuthal resolutions more exactly than can be done with spherical harmonics. However, the spatial smoothing leaves some non-negligible power at higher degrees and orders, and results in instabilities in the basin center where the azimuthal smoothing has no effect. In terms of the locations and character of the ring fault signatures, the results of the spatial smoothing models are consistent with the spherical harmonic smoothing models (c.f., Fig. 7d and Fig. A4b). However, the spatial smoothing models were found to generate more ring-like artifacts by artificially stretching anomalies in the azimuthal direction. Although we opt to use the spherical harmonic smoothing approach for our main analysis, these spatial smoothing models confirm that our results are not a byproduct of our novel degree- and order-dependent spherical harmonic filtering. A number of other filtering approaches were also tested, including separate degree-dependent and order-dependent cosine-shaped tapers, and found to perform poorly.

A number of additional tests were performed on the model. To ensure that the ring-like structures are not numerical ringing around the central positive Bouguer anomaly, we generated models in which we flattened out the central positive Bouguer anomaly by interpolating inward from its edge, and then repeated the crustal thickness modeling. The results of these models were nearly indistinguishable from the original models at the rings. We also performed tests in which we flattened out the Bouguer gravity outside the central positive Bouguer anomaly and repeated the crustal thickness modeling. These models produced a small amount of numerical ringing in the crustal thickness model immediately outside the central mantle uplift, but the

amplitude and location of this ringing did not match the ring structures observed around the basin in the original models.

References.

Anderson, E.M., 1905. The dynamics of faulting. Trans. Edinburgh Geol. Soc. 387–402.

Andrews-Hanna, J.C., 2013. The origin of the non-mare mascon gravity anomalies in lunar basins. Icarus 222, 159–168. doi:10.1016/j.icarus.2012.10.031

Andrews-Hanna, J.C., Asmar, S.W., Head, J.W., Kiefer, W.S., Konopliv, A.S., Lemoine, F.G., Matsuyama, I., Mazarico, E., McGovern, P.J., Melosh, H.J., Neumann, G. a, Nimmo, F., Phillips, R.J., Smith, D.E., Solomon, S.C., Taylor, G.J., Wieczorek, M.A., Williams, J.G., Zuber, M.T., 2013a. Ancient igneous intrusions and early expansion of the Moon revealed by GRAIL gravity gradiometry. Science 339, 675–678. doi:10.1126/science.1231753

Andrews-Hanna, J.C., Besserer, J., Head III, J.W., Howett, C.J.A., Kiefer, W.S., Lucey, P.J., McGovern, P.J., Melosh, H.J., Neumann, G.A., Phillips, R.J., Schenk, P.M., Smith, D.E., Solomon, S.C., Zuber, M.T., 2014. Structure and evolution of the lunar Procellarum region as revealed by GRAIL gravity data. Nature 514, 68–71. doi:10.1038/nature13697

Andrews-Hanna, J.C., Freed, A.M., Head, J.W., Melosh, H.J., Neumann, G.A., Soderblom, J.M., Wieczorek, M.A., Zuber, M.T., 2013b. The compensation state and ring structures of lunar basins as revealed by GRAIL gravity. Lunar Planet Sci. Conf. 44, Abstract 2823.

Baker, D.M.H., Head, J.W., Collins, G.S., Potter, R.W.K., 2015. The formation of peak-ring basins: Working hypotheses and path forward in using observations to constrain models of impact-basin formation. Icarus. doi:10.1016/j.icarus.2015.11.033

Baker, D.M.H., Head, J.W., Fassett, C.I., Kadish, S.J., Smith, D.E., Zuber, M.T., Neumann, G.A., 2011. The transition from complex crater to peak-ring basin on the Moon : New observations from the Lunar Orbiter Laser Altimeter (LOLA) instrument. Icarus 214, 377–393. doi:10.1016/j.icarus.2011.05.030

Baker, D.M.H., Head, J.W., Neumann, G. A., Smith, D.E., Zuber, M.T., 2012. The transition from complex craters to multi-ring basins on the Moon: Quantitative geometric properties from Lunar Reconnaissance Orbiter Lunar Orbiter Laser Altimeter (LOLA) data. J. Geophys. Res. 117. doi:10.1029/2011JE004021

Baker, D.M.H., Head, J.W., Phillips, R.J., Neumann, G.A., Bierson, C.J., Smith, D.E., Zuber, M.T., 2017. GRAIL gravity observations of the transition from complex crater to peak-ring basin on the Moon : Implications for crustal structure and impact basin formation 292, 54–73. doi:10.1016/j.icarus.2017.03.024

Baldwin, R.B., 1972. The tsunami model of the origin of ring structures concentric with large lunar craters. Phys. Earth Planet. Inter. 6, 327–339.

Besserer, J., Nimmo, F., Wieczorek, M.A., Weber, R.C., Kiefer, W.S., Mcgovern, P.J., Andrews-Hanna, J.C., Smith, D.E., Zuber, M.T., 2014. GRAIL gravity constraints on the vertical and lateral density structure of the lunar crust. Geophys. Res. Lett. 41, 5771–5777. doi:10.1002/2014GL060240.1.

Beutner, E.C., Gerbi, G.P., 2005. Catastrophic emplacement of the Heart Mountain block slide, Wyoming and Montana, USA. Geol. Soc. Am. Bull. 117, 724–735. doi:10.1130/B25451.1

Byrne, P.K., Klimczak, C., McGovern, P.J., Mazarico, E., James, P.B., Neumann, G.A., Zuber, M.T., Solomon, S.C., 2015. Deep-seated thrust faults bound the Mare Crisium lunar mascon. Earth Planet. Sci. Lett. 427, 183–190. doi:10.1016/j.epsl.2015.06.022

Christeson, G.L., Collins, G.S., Morgan, J. V., Gulick, S.P.S., Barton, P.J., Warner, M.R., 2009. Mantle deformation beneath the Chicxulub impact crater. Earth Planet. Sci. Lett. 284, 249–257. doi:10.1016/j.epsl.2009.04.033

Cole, H.M., Andrews-Hanna, J.C., 2017. The anatomy of a wrinkle ridge revealed in the wall of Melas Chasma, Mars. J. Geophys. Res. Planets 122, 889–900, doi:10.1002/2017JE005274.

Cowie, P.A., Scholz, C.H., 1992. Physical explanation for the displacement-length relationship of faults using a post-yield fracture mechanics model. J. Struct. Geol. 14, 1133–1148. doi:10.1016/0191-8141(92)90065-5

Fassett, C.I., Head, J.W., Baker, D.M.H., Zuber, M.T., Smith, D.E., Neumann, G.A., Solomon, S.C., Klimczak, C., Strom, R.G., Chapman, C.R., Prockter, L.M., Phillips, R.J., Oberst, J., Preusker, F., 2012. Large impact basins on Mercury: Global distribution, characteristics, and modification history from MESSENGER orbital data. J. Geophys. Res. 117, E00L08. doi:10.1029/2012JE004154

Fassett, C.I., Head, J.W., Smith, D.E., Zuber, M.T., Neumann, G.A., 2011. Thickness of proximal ejecta from the Orientale Basin from Lunar Orbiter Laser Altimeter (LOLA) data: Implications for multi-ring basin formation. Geophys. Res. Lett. 38, L17201. doi:10.1029/2011GL048502

Forsberg, R., 1984. A study of terrain corrections, density anomalies, and geophysical inversion methods in gravity field modeling. Rep. 355, Dep. Geod. Sci. Surv. Ohio State Univ.

Freed, A.M., Johnson, B.C., Blair, D.M., Melosh, H.J., Neumann, G.A., Phillips, R.J., Solomon, S.C., Wieczorek, M.A., Zuber, M.T., 2014. The formation of lunar mascon basins from impact to contemporary form. J. Geophys. Res. Planets 119, doi:10.1002/2014JE004657.

Gaffney, E.S., Damjanac, B., Valentine, G.A., 2007. Localization of volcanic activity: 2. Effects of pre-existing structure. Earth Planet. Sci. Lett. 263, 323–338. doi:10.1016/j.epsl.2007.09.002

Gulick, S.P.S., Barton, P.J., Christeson, G.L., Morgan, J. V., McDonald, M., Mendoza-Cervantes, K., Pearson, Z.F., Surendra, A., Urrutia-Fucugauchi, J., Vermeesch, P.M., Warner, M.R., 2008. Importance of pre-impact crustal structure for the asymmetry of the Chicxulub impact crater 131–135. doi:10.1038/ngeo103

Gulick, S.P.S., Christeson, G.L., Barton, P.J., Grieve, R.A.F., Morgan, J. V, Urrutia-Fucugauchi, J., 2013. Geophysical characterization of the Chicxulub impact crater. Rev. Geophys. 51, 31–52. doi:10.1002/rog.20007.1.

Hartmann, W.K., Kuiper, G.P., 1962. Concentric structure surrounding lunar basins. Comm. Lunar Planet. Lab. 1, 51–66.

Hartmann, W.K., Wood, C.A., 1971. Moon: Origin and evolution of multi-ring basins. Moon 3, 3–78.

Head, J.W., 2010. Transition from complex craters to multi-ringed basins on terrestrial planetary

bodies: Scale-dependent role of the expanding melt cavity and progressive interaction with the displaced zone. Geophys. Res. Lett. 37, 1–5. doi:10.1029/2009GL041790

Head, J.W., 1974. Orientale multi-ringed basin interior and implications for petrogenesis of lunar highland samples. Moon 11, 327–356.

Head, J.W., Wilson, L., 2017. Generation, ascent and eruption of magma on the Moon: New Insights into source depths , magma supply, intrusions and effusive/explosive eruptions (Part 2: Predicted emplacement processes and observations). Icarus 283, 146–175. doi:10.1016/j.icarus.2016.05.031

Head, J.W., Wilson, L., Weitz, C.M., 2002. Dark ring in southwestern Orientale Basin : Origin as a single pyroclastic eruption. J. Geophys. Res. 107, 5001. doi:10.1029/2000JE001438

Hodges, C.A., Wilhelms, D.E., 1978. Formation of lunar basin rings. Icarus 34, 294–323.

Ishihara, Y., Goossens, S., Matsumoto, K., Noda, H., Araki, H., Namiki, N., Hanada, H., Iwata, T., Tazawa, S., Sasaki, S., 2009. Crustal thickness of the Moon: Implications for farside basin structures. Geophys. Res. Lett. 36, 1–4. doi:10.1029/2009GL039708

Jansen, J.C., Andrews-Hanna, J.C., Li, Y., Lucey, P.G., Taylor, G.J., Goossens, S., Lemoine, F.G., Mazarico, E., Head, J.W., Milbury, C., Kiefer, W.S., Soderblom, J.M., Zuber, M.T., 2017. Small-scale density variations in the lunar crust revealed by GRAIL. Icarus 291, 107–123. doi:10.1016/j.icarus.2017.03.017

Johnson, B.C., Blair, D.M., Collins, G.S., Melosh, H.J., Freed, A.M., Taylor, G.J., Head, J.W., Wieczorek, M.A., Andrews-hanna, J.C., Nimmo, F., Keane, J.T., Miljkovi, K., Soderblom, J.M., Zuber, M.T., 2016. Formation of the Orientale lunar multiring basin. Science 354, 441–444.

Jozwiak, L.M., Head, J.W., Neumann, G.A., Wilson, L., 2017. Observational constraints on the identification of shallow lunar magmatism: Insights from floor-fractured craters. Icarus 283, 224–231. doi:10.1016/j.icarus.2016.04.020

Jozwiak, L.M., Head, J.W., Wilson, L., 2015. Lunar floor-fractured craters as magmatic intrusions: Geometry, modes of emplacement, associated tectonic and volcanic features, and implications for gravity anomalies. Icarus 248, 424–447. doi:10.1016/j.icarus.2014.10.052

Kattoum, Y.N., Andrews-Hanna, J.C., 2013. Evidence for ring-faults around the Orientale basin on the Moon from gravity. Icarus 226, 694–707. doi:10.1016/j.icarus.2013.06.025

Kiefer, W.S., MacKe, R.J., Britt, D.T., Irving, A.J., Consolmagno, G.J., 2012. The density and porosity of lunar rocks. Geophys. Res. Lett. 39, L07201. doi:10.1029/2012GL051319

Konopliv, A.S., Park, R.S., Yuan, D.N., Asmar, S.W., Watkins, M.M., Williams, J.G., Fahnestock, E., Kruizinga, G., Paik, M., Strekalov, D., Harvey, N., Smith, D.E., Zuber, M.T., 2014. High-resolution lunar gravity fields from the GRAIL Primary and Extended Missions. Geophys. Res. Lett. 41, 1452–1458. doi:10.1002/2013GL059066

Kreslavsky, M.A., Head, J.W., 2012. New observational evidence of global seismic effects of basin-forming impacts on the Moon from lunar reconnaissance orbiter lunar orbiter laser altimeter data. J. Geophys. Res. 117, E00H24. doi:10.1029/2011JE003975

Kring, D.A., Kramer, G.Y., Collins, G.S., Potter, R.W.K., Chandnani, M., 2016. Peak-ring structure and kinematics from a multi-disciplinary study of the Schrodinger impact basin. Nat. Commun. 7, 13161, doi:10.1038/ncomms13161.

Li, X., Chouteau, M., 1998. Three-dimensional gravity modeling in all space. Surv. Geophys. 3, 339–368. doi:10.1190/1.1885936

McGovern, P.J., Kiefer, W.S., Kramer, G.Y., Zuber, M.T., Andrews-Hanna, J.C., Head, J.W., 2014. Magma ascent at lunar impact basins: Effects of lithospheric tectonic stress gradients, brittle failure, and volatile generation. Lunar Planet. Sci. Conf. 45, Abstract 2771.

Melosh, H.J., 1982. A simple mechanical model of Valhalla basin, Callisto. J. Geophys. Res. 87, 1880–1890.

Melosh, H.J., Freed, A.M., Johnson, B.C., Blair, D.M., Andrews-Hanna, J.C., Neumann, G.A., Phillips, R.J., Smith, D.E., Solomon, S.C., Wieczorek, M.A., Zuber, M.T., 2013. The origin of lunar mascon basins. Science 340, 1552–1556.

Melosh, H.J., Mckinnon, W.B., 1978. The mechanics of ringed basin formation. Geophys. Res. Lett. 5, 8–11.

Metropolis, N., Rosenbluth, A.W., Rosenbluth, M.N., Teller, A.H., Teller, E., 1953. Equations of state calculations by fast computing machine. J. Chem. Phys. 21, 1087–1091.

Morgan, J. V, Gulick, S.P.S., Bralower, T., Chenot, E., Christeson, G., Claeys, P., Cockell, C., Collins, G.S., Coolen, M.J.L., Ferrière, L., Gebhardt, C., Goto, K., Jones, H., Kring, D.A., Le Ber, E., Lofi, J., Long, X., Lowery, C., Mellett, C., Ocampo-Torres, R., Osinski, G.R., Perez-Cruz, L., Pickersgill, A., Poelchau, M., Rae, A., Rasmussen, C., Rebolledo-Vieyra, M., Riller, U., Sato, H., Schmitt, D.R., Smit, J., Tikoo, S., Tomioka, N., Urrutia-Fucugauchi, J., Whalen, M., Wittmann, A., Yamaguchi, K.E., Zylberman, W., 2016. The formation of peak rings in large impact craters. Science 354, 878–882.

Nahm, A.L., Öhman, T., Kring, D. a., 2013. Normal faulting origin for the cordillera and outer rook rings of orientale basin, the moon. J. Geophys. Res. E Planets 118, 190–205. doi:10.1002/jgre.20045

Neumann, G.A., Zuber, M.T., Smith, D.E., Lemoine, F.G., 1996. The lunar crust: Global structure and signature of major basins. J. Geophys. Res. 101, 16,841-16,843.

Neumann, G.A., Zuber, M.T., Wieczorek, M.A., Head, J.W., Baker, D.M.H., Solomon, S.C., Smith, D.E., Lemoine, F.G., Mazarico, E., Sabaka, T.J., Goossens, S.J., Melosh, H.J., Phillips, R.J., Asmar, S.W., Konopliv, A.S., Williams, J.G., Sori, M.M., Soderblom, J.M., Miljkovi, K., Andrews-hanna, J.C., Nimmo, F., Kiefer, W.S., 2015a. Lunar impact basins revealed by Gravity Recovery and Interior Laboratory measurements. Sci. Adv. 1, 1:e1500852.

Neumann, G.A., Zuber, M.T., Wieczorek, M.A., Head, J.W., Baker, D.M.H., Solomon, S.C., Smith, D.E., Lemoine, F.G., Mazarico, E., Sabaka, T.J., Goossens, S.J., Melosh, H.J., Phillips, R.J., Asmar, S.W., Konopliv, A.S., Williams, J.G., Sori, M.M., Soderblom, J.M., Miljkovi, K., Andrews-Hanna, J.C., Nimmo, F., Kiefer, W.S., 2015b. Lunar impact basins revealed by Gravity Recovery and Interior Laboratory measurements. Sci. Adv. 1, e1500852.

Potter, R.W.K., 2015. Investigating the onset of multi-ring impact basin formation. Icarus 261, 91–99. doi:10.1016/j.icarus.2015.08.009

Potter, R.W.K., Kring, D.A., Collins, G.S., Kiefer, W.S., Mcgovern, P.J., 2013. Numerical modeling of the formation and structure of the Orientale impact basin. J. Geophys. Res. 118, 963–979. doi:10.1002/jgre.20080

Schultz, P.H., Papamarcos, S., 2010. Evolving flowfields from the Imbrium and Orientale impacts. Lunar Planet. Sci. Conf. 41, Abstract 2480.

Schultz, R.A., Frey, H. V., 1990. A new survey of multiring impact basins on Mars. J. Geophys. Res. 95, 14,175-14,189. doi:10.1029/JB095iB09p14175

Smith, D.E., Zuber, M.T., Neumann, G.A., Lemoine, F.G., Mazarico, E., Torrence, M.H., McGarry, J.F., Rowlands, D.D., Head, J.W., Duxbury, T.H., Aharonson, O., Lucey, P.G., Robinson, M.S., Barnouin, O.S., Cavanaugh, J.F., Sun, X., Liiva, P., Mao, D.D., Smith, J.C., Bartels, A.E., 2010. Initial observations from the Lunar Orbiter Laser Altimeter (LOLA). Geophys. Res. Lett. 37, L18204, doi:10.1029/2010GL043751. doi:10.1029/2010GL043751

Solomon, S.C., Head, J.W., 1980. Lunar mascon basins - Lava filling, tectonics, and evolution of the lithosphere. doi:10.1029/RG018i001p00107

Solomon, S.C., Head, J.W., 1979. Vertical movement in mare basins: Relation to mare emplacement, basin tectonics, and lunar thermal history. J. Geophys. Res. 84, 1667–1682. doi:10.1029/JB084iB04p01667

Spudis, P.D., 1993. The Geology of Multi-Ring Impact Basins. Cambridge University Press.

Spudis, P.D., Guest, J.E., 1988. Stratigraphy and geologic history of Mercury, in: Mercury. University of Arizona Press, Tucson, pp. 118–164.

Spudis, P.D., Martin, D.J.P., Kramer, G., 2014. Geology and composition of the orientale basin impact melt sheet. J. Geophys. Res. E Planets 119, 19–29. doi:10.1002/2013JE004521

Thorey, C., Michaut, C., Wieczorek, M., 2015. Gravitational signatures of lunar floor-fractured craters. Earth Planet. Sci. Lett. 424, 269–279. doi:10.1016/j.epsl.2015.04.021

Vaughan, W.M., Head, J.W., Wilson, L., Hess, P.C., 2013. Geology and petrology of enormous volumes of impact melt on the Moon: A case study of the Orientale basin impact melt sea. Icarus 223, 749–765. doi:10.1016/j.icarus.2013.01.017

Vermeesch, P.M., Morgan, J. V, 2008. Structural uplift beneath the Chicxulub impact structure. J. Geophys. Res. 113, B07103, doi:10.1029/2007JB005393.

Whitten, J., Head, J.W., Staid, M., Pieters, C.M., Mustard, J., Clark, R., Nettles, J., Klima, R.L., Taylor, L., 2011. Lunar mare deposits associated with the Orientale impact basin: New insights into mineralogy, history, mode of emplacement, and relation to Orientale Basin evolution from Moon Mineralogy Mapper (M3) data from Chandrayaan-1. J. Geophys. Res. 116, E00G09, doi:10.1029/2010JE003736.

Wieczorek, M.A., 2014. SHTOOLS - Tools for working with spherical harmonics (v2.9.1). Zenodo. doi:10.5281/zenodo.12158

Wieczorek, M.A., Neumann, G.A., Nimmo, F., Kiefer, W.S., Taylor, G.J., Melosh, H.J., Phillips, R.J., Solomon, S.C., Andrews-Hanna, J.C., Asmar, S.W., Konopliv, A.S., Lemoine, F.G., Smith, D.E., Watkins, M.M., Williams, J.G., Zuber, M.T., 2013. The crust of the Moon as seen by GRAIL. Science 339, 671–675. doi:10.1126/science.1231530

Wieczorek, M.A., Phillips, R.J., 1999. Lunar multiring basins and the cratering process. Icarus 139, 246–259. doi:10.1006/icar.1999.6102

Wieczorek, M.A., Phillips, R.J., 1998. Potential anomalies on a sphere: Applications to the thickness of the lunar crust. J. Geophys. Res. 103, 1715–1724.

Wieczorek, M. a., 2007. Gravity and topography of the terrestrial planets. Treatise Geophys. 10, 165–206. doi:10.1016/B978-044452748-6.00156-5

Wieczorek, M. a., 2006. The constitution and structure of the lunar interior. Rev. Mineral. Geochemistry 60, 221–364. doi:10.2138/rmg.2006.60.3

Wilhelms, 1987. The Geologic History of the Moon, U.S. Geol. Surv. Prof. Pap. 13.

Wilson, L., Head, J.W., 2011. Impact melt sheets in lunar basins: Estimating thickness from cooling behavior. Lunar Planet. Sci. Conf. 42, Abstract 1345. doi:10.1029/2010GL043751

Wilson, L., Head, J.W., 1981. Ascent and eruption of basaltic magma on the Earth and Moon 86, 2971–3001. doi:10.1029/JB086iB04p02971

Zeng-Yuan, Y., Bin, Z., Dao-Han, C., 1990. On the tsunami model of the origin of multi-ring basins. Earth, Moon Planets 49, 253–258.

Zuber, M.T., Smith, D.E., Lehman, D.H., Hoffman, T.L., Asmar, S.W., Watkins, M.M., 2013a. Gravity Recovery and Interior Laboratory (GRAIL): Mapping the lunar interior from crust to core. Space Sci. Rev. 178, 3–24. doi:10.1007/s11214-012-9952-7

Zuber, M.T., Smith, D.E., Lemoine, F.G., Neumann, G.A, 1994. The shape and internal structure of the moon from the clementine mission. Science 266, 1839–1843. doi:10.1126/science.266.5192.1839

Zuber, M.T., Smith, D.E., Neumann, G.A., Goossens, S.J., Andrews-Hanna, J.C., Head, J.W., Kiefer, W.S., Asmar, S.W., Konopliv, A.S., Lemoine, F.G., Matsuyama, I., Melosh, H.J., Mcgovern, P.J., Nimmo, F., Phillips, R.J., Solomon, S.C., Taylor, G.J., Watkins, M.M., Wieczorek, M.A., Williams, J.G., Jansen, J.C., Johnson, B.C., Keane, J.T., Mazarico, E., Miljković, K., Park, R.S., Soderblom, J.M., Yuan, D.-N., 2016. Gravity field of the Orientale basin from the Gravity Recovery and Interior Laboratory (GRAIL) mission. Science 354, 438–441.

Zuber, M.T., Smith, D.E., Watkins, M.M., Asmar, S.W., Konopliv, A.S., Lemoine, F.G., Melosh, H.J., Neumann, G.A., Phillips, R.J., Solomon, S.C., Wieczorek, M. a, Williams, J.G., Goossens, S.J., Kruizinga, G., Mazarico, E., Park, R.S., Yuan, D.-N., 2013b. Gravity Field of the Moon from the Gravity Recovery and Interior Laboratory (GRAIL) Mission. Science 668, 1–5. doi:10.1126/science.1231507